The Journal of Physiology

Computational analysis to assess hemodynamic forces in descending thoracic aortic aneurysms

Francesca Duca[1], Daniele Bissacco[2,3], Luca Crugnola[1], Chiara Faitini[4], Maurizio Domanin[2,3], Francesco Migliavacca[1], Santi Trimarchi[2,3] and Christian Vergara[1]

[1]*LaBS, Dipartimento di Chimica, Materiali e Ingegneria Chimica, Politecnico di Milano, Milan, Italy*
[2]*Department of Clinical Sciences and Community Health, Università degli Studi di Milano, Milan, Italy*
[3]*Section of Vascular Surgery, Cardio Thoracic Vascular Department, Fondazione I.R.C.C.S. Ca' Granda Ospedale Maggiore Policlinico, Milan, Italy*
[4]*Mines Paris-PSL, Paris, France*

Handling Editors: Natalia Trayanova & T. Alexander Quinn

The peer review history is available in the Supporting Information section of this article (https://doi.org/10.1113/JP287278#support-information-section).

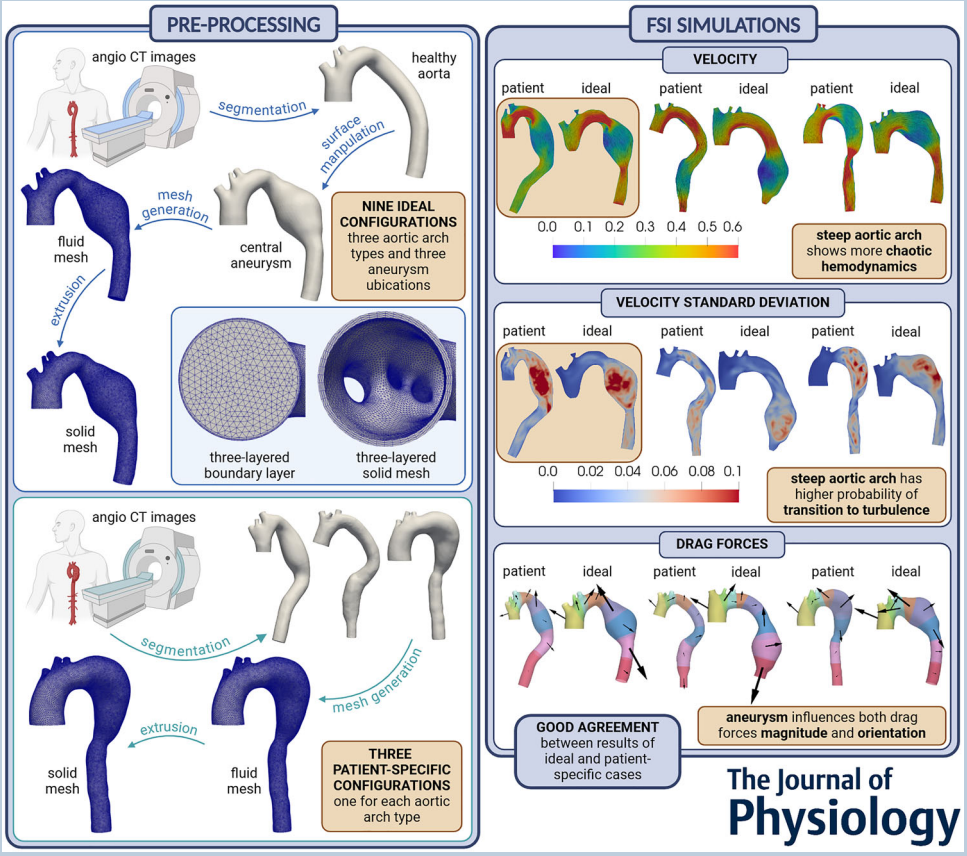

Abstract figure legend Left: Pre-processing. First, we perform the segmentation of the Computer Tomography angiorgraphy (angio-CT) scans of a healthy patient, obtaining the surface of a healthy thoracic aorta with a Type III aortic arch. Then, we build nine ideal configurations with Descending Thoracic Aortic Aneurysm (DTAA), varying the aortic arch type and the aneurysm ubication, by manipulating the segmented surface. Then, for each ideal configuration, we generate the fluid mesh with a three-layered boundary layer and, by extruding the external fluid surface, we generate a three-layered solid mesh. By segmenting the angio-CT imagies of three patients, we are able to reconstruct three patient-specific configurations, which correspond to three of the ideal configurations. Then, as for the ideal configurations, for each patient-specific geometry, we generate a fluid mesh with three-layered boundary layer and a three-layered solid mesh. Right: Fluid-Structure Interaction (FSI) simulations results. (Top) Blood velocity at the systolic

 DOI: 10.1113/JP287278

peak shows that configurations with a steeper aortic arch present a more chaotic hemodynamics with greater vortices. (Centre) The standard deviation of velocity at early systole exhibits higher values in configurations with steep aortic arch. Accordingly, the latter have higher probability to develop transition to turbulence. (Bottom) The regions including DTAA show great drag forces magnitude, and regions including the aneurysm necks present drag forces mainly oriented towards the vessel centerline. All the cases presented show off the great accordance between the results of the patient-specific and the corrseponding ideal configurations.

Abstract Descending thoracic aortic aneurysm (DTAA) is a life-threatening disorder, defined as a localized enlargement of the descending portion of the thoracic aorta. In this context, we develop a fluid–structure interaction (FSI) computational framework, with the inclusion of a turbulence model and different material properties for the healthy and the aneurysmatic portions of the vessel, to study the hemodynamics and its relationship with DTAA. We first provide an analysis on nine ideal scenarios, accounting for different aortic arch types and DTAA ubications, to study changes in blood pressure, flow patterns, turbulence, wall shear stress, drag forces and internal wall stresses. Our findings demonstrate that the hemodynamics in DTAA is profoundly disturbed, with the presence of flow re-circulation, formation of vortices and transition to turbulence. In particular, configurations with a steeper aortic arch exhibit a more chaotic hemodynamics. We notice also an increase in pressure values for configurations with less steep aortic arch and in drag forces for configurations with distal DTAA. Second, we replicate our analysis for three patient-specific cases (one for type of arch) obtaining comforting results in terms of accordance with the ideal scenarios. Finally, in a very preliminary way, we try to relate our findings to possible stent-graft migrations after TEVAR procedure to provide predictions on the postoperative state.

(Received 21 November 2024; accepted after revision 20 March 2025; first published online 15 May 2025)
Corresponding author Christian Vergara, LaBS, Dipartimento di Chimica, Materiali e Ingegneria Chimica, Politecnico di Milano, Piazza Leonardo da Vinci 32, 20133 Milan, Italy.
Email: christian.vergara@polimi.it

Key points

- This study employs computational methods to assess hemodynamic forces in descending thoracic aortic aneurysms.
- We consider ideal cases by varying aortic arch type and aneurysm location.
- Our results show: chaotic hemodynamics for steep aortic arches; increase in pressure values for less steep aortic arches; high risk of plaque deposition in the aneurysmal sac for proximal aneurysms and near the neck for distal aneurysms.
- We also analyse three patient-specific cases, confirming the major outcomes found for the ideal cases.
- We try to suggest how our preoperative findings may correlate to assess the risk of stent-graft migration of a possible TEVAR procedure.

Francesca Duca received her BSc and MSc in Biomedical Engineering at Politecnico di Milano in Italy. She is currently pursuing her PhD in Bioengineering at Politecnico di Milano under the supervision of Professor Christian Vergara and Professor Francesco Migliavacca. Her PhD is funded by the Italian Ministry of Education, and it concerns the use of computational methodologies for a better decision making process in vascular surgery. Specifically, her research is now focused on the development of a computational framework to assess the pre-operative hemodynamics aiming to improve Thoracic Endovascular Aortic Repair (TEVAR) outcomes.

Introduction

Thoracic aortic aneurysm (TAA) is one of the most serious and potentially fatal diseases regarding the aorta. Descending thoracic aortic aneurysm (DTAA) is defined as a localized increase in the descending segment of the thoracic aorta (TA) diameter of at least 50% with respect to the same aortic segment in age-matched and sex-matched healthy individuals (Bossone & Eagle, 2021). Even though DTAA pathophysiology is still poorly understood, from a histopathologic point of view, aneurysm formation may involve an alteration of the quantity and architecture of the tunica media components of descending thoracic aorta (DTA), namely elastin, collagen fibres and smooth muscle cells (Goldfinger et al., 2014). This degenerative process leads to a progressive remodelling, which induces a diminished aortic resilience and tensile strength, aortic wall thinning, increased wall stresses and further aneurysm dilation, all of which could ultimately culminate in catastrophic events such as dissection and/or aneurysm rupture (Clift & Cervi, 2020).

Currently, there are two available surgical procedures for DTAA treatment: the open surgical strategy and the Thoracic endovascular aortic repair (TEVAR). Specifically, TEVAR is a minimally invasive strategy based on aneurysm sac exclusion and depressurization through the deployment of a self-expandable stent-graft, and secure endograft fixation in correspondence of normal aorta proximal and distal zones of attachment, known as *landing zones*. This minimally invasive procedure represents a well-established alternative to open repair in individuals with suitable anatomic features, particularly in patients considered at high surgical risk but with a reasonable life expectancy after the procedure (Marrocco-Trischitta et al., 2009).

Clinical guidelines suggest surgical intervention for DTAA when its diameter is $\geq$ 60 mm or expands at a rate $\geq$ 5 mm/year (Riambau et al., 2017). However there still remains a significant incidence of adverse events in patients whose aortas are smaller than these intervention thresholds (Elefteriades & Farkas, 2010). Thus several prognostic factors have been discussed to better investigate and predict aneurysm progression and/or rupture (Fillinger et al., 2003; Mourato et al., 2022; Venkatasubramaniam et al., 2004). Among these, hemodynamic parameters comprise a useful tool in analysing and quantifying the risk of negative outcomes in DTAA (Mandigers et al., 2023; Shang et al., 2013). In fact, aneurysm development has been associated with adverse vascular remodelling, induced by complex flow dynamics and abnormal Wall shear stress (WSS), which tends to be lower than in healthy aortic segments (Peattie et al., 2004). In particular, hemodynamics in DTAA is profoundly disturbed, presenting flow re-circulation, vortex formation and adverse WSS, all of which possibly lead to further aneurysm growth and progressive aortic wall thinning, weakening and even rupture (Tan et al., 2009). Accordingly the knowledge of the local hemodynamics in DTAAs may improve aneurysm expansion and rupture risk assessment.

Nowadays computational modelling has become a valuable tool to simulate and analyse complex hemodynamics in the cardiovascular system (Boyd et al., 2016; Carpenter et al., 2020, 2023; Wang et al., 2023), providing new insights into the mechanisms and pathophysiology of artery diseases, such as aortic aneurysm (Boussel et al., 2008; Doyle et al., 2009; Vorp et al., 1998). Computational modelling can be used to precisely quantify the blood flow characteristics, wall forces and wall displacements in aortic aneurysms, using either a rigid wall assumption (Frauenfelder et al., 2006; Soudah et al., 2013; Tse et al., 2011) (Computational fluid dynamics – CFD) or a fluid–structure interaction (FSI) approach (Borghi et al., 2008; Di Martino et al., 2001; Scotti et al., 2005), where the vessel compliance is accounted for.

Even though there are many works that focused on hemodynamics and WSS in presence of both abdominal (Biasetti et al., 2010; Molony et al., 2009; Piccinelli et al., 2013; Wolters et al., 2005) and ascending TAAs (Callaghan et al., 2015; Campobasso et al., 2018; Etli et al., 2021; Pasta et al., 2013), DTAAs have been poorly investigated by computational modelling. CFD experiments in Numata et al. (2016) showed for two DTAA patients very low velocity values within the aneurysm, as well as the presence of a vortical flow in systole, leading to transition to turbulence in the ascending aorta and high oscillatory shear index (OSI) areas, which might be associated with atherosclerotic plaque formation. Duronio and Di Mascio (2023) employed CFD to compare the flow patterns in normal and DTAA subjects. Their findings demonstrated that in the aneurysmatic aorta blood flow was unstable with re-circulation regions within the aneurysm, causing prolonged contact between blood particles and the aneurysm lumen surface, potentially leading to plaque deposition.

When the vascular district undergoes relatively large displacements, like TA, the rigid wall assumption characterizing CFD could be substituted by FSI modelling, which may improve the hemodynamic description (Reymond et al., 2013). For instance, in TA, the computational experiment conducted by Crosetto et al. (2011) demonstrated that the rigid wall assumption tends to overestimate WSS values, when compared to FSI. Similarly, in abdominal aortic aneurysms, Lin et al. (2017) found that the rigid wall assumption of CFD significantly affected the blood flow patterns reducing the size of vortices, which in turn impeded the energy dissipation into the aneurysm wall, increased the turbulent kinetic energy at the vortex region and finally lead to the overestimation of WSS at the proximal neck region. Moreover, unlike CFD, the FSI approach permits also to model the

aortic wall dynamics, providing valuable information on the state of stress of the wall (Mendez et al., 2018) and on the disease progression (Valente et al., 2022). In this regard Tan et al. (2009) demonstrated that the FSI approach may provide a clearer insight into the development of DTAA, if compared with CFD modelling (Tan et al., 2009), allowing to examine the effects of factors such as geometrical features and wall composition on blood velocity and wall stress. In the context of FSI for DTAA, Ong et al. (2019) compared hemodynamic quantities in a healthy and a DTAA case, Silva et al. (2023) investigated maximum stress and displacement of the arterial wall and Dadras et al. (2023) compared different hemodynamic and structural parameters before and after TEVAR, finding a significant improvement in velocity and pressure distribution and the damping of swirling flows strength after stenting. Notwithstanding the above, it is important to point out that FSI modelling can dramatically increase the computational cost, which might pose a problem for certain clinical applications.

Previous studies highlighted that the magnitude and orientation of *drag forces* may identify landing zones with a hostile biomechanical environment (Marrocco-Trischitta et al., 2019), which therefore may cause an insufficient proximal seal or migration of the endoprosthesis used in TEVAR (Marrocco-Trischitta et al., 2020). In this regard, while there are several studies that used CFD to investigate drag forces after the stent-graft deployment (Fung et al., 2008; Figueroa & Zarins, 2011; Krsmanovic et al., 2014), there are few works that focus on the preoperative scenario (Belvroy et al., 2020; Marrocco-Trischitta et al., 2019), and none of these exploits FSI. Domanin et al. (2021) highlighted the predictive potential of the preoperative analysis, describing a case report in which the proximal landing zone of the endoprosthesis was chosen according to the preoperative computation of drag forces, by means of CFD, and 6 months follow-up computed tomography angiography (CTA) confirmed the validity of that decision.

In this study we develop an FSI computational framework to investigate the flow patterns and the wall motion in 12 highly representative scenarios, encompassing the three types of aortic arch (i.e. Type I, Type II and Type III (Madhwal et al., 2008)) and three different aneurysmatic configurations, all obtained by virtual manipulation of CTA images of one healthy patient (referred in what follows as *virtual ideal cases*). The first aim of this work is to estimate, for each scenario, several hemodynamic quantities (i.e. blood pressure and velocity, turbulence, OSI and drag forces (Marrocco-Trischitta et al., 2018)), as well as vessel wall internal stresses. On the basis of this computational analysis, we are able to provide a comparison among the various scenarios, quantifying the differences between the pathological and the healthy cases, in terms of hemodynamic forces and wall stresses.

The second purpose of this work is to apply the previous analysis to three *DTAA patient-specific cases* with similar configurations to some of the idealized scenarios to demonstrate the validity of the results obtained in the latter cases. Specifically, we exploit the aforementioned preoperative analysis with the aim of creating a link between preoperative drag forces and the optimal landing zones for the stent-graft anchoring for the patient-specific cases. Thus for each diseased configuration, we are able to identify which landing zones might be the most hemodynamically disturbed and, for this reason, should be avoided for stent-graft sealing.

The main novelties of this study rely on (i) the parametric analysis of hemodynamics in DTAA for different arch types and aneurysm locations; (ii) the use of different vessel compliance in FSI simulations for healthy and aneurysmatic wall; and (iii) the use of a turbulence model to assess transition to turbulence in DTAA. Notice also that, in the context of the computational evaluation of the hemodynamics in presence of aortic aneurysms, the majority of the literature works are mainly focused on abdominal or ascending TA aneurysms.

Materials and methods

Generation of computational scenarios

In this study the pre-processing phase allowed us to build *virtual ideal* and *patient-specific* geometries and meshes as described in what follows.

Virtual geometries. Here we focus on the development of virtual thoracic aortic models with three distinct arch types (i.e. Type I, Type II and Type III), according to the Aortic Arch Classification (Madhwal et al., 2008), and differently located fusiform aneurysms along the descending portion of the vessel (i.e. proximal, central and distal). Thus, 12 TA scenarios were developed: three healthy configurations, one for each arch type, and nine with a DTAA located in the proximal, central or distal DTA, further divided based on the arch type.

The starting point was a healthy TA with a Type III aortic arch, obtained from the segmentation of CTA images of a 40-year-old man taken at Fondazione IRCCS Ca' Granda Ospedale Maggiore – Policlinico di Milano (all patient's data were anonymized by a staff physician before the computational analysis). CTA scans were performed using a Siemens Somatom Definition Flash scanner (Siemens Healthineers, Forchheim, Germany) with the following acquisition parameters: slice thickness of 0.75 mm, reconstruction matrix of 512 × 512 pixels and in-plane resolution of 0.396 mm × 0.396 mm. A level-set technique with a colliding fronts initialization, provided by the *Vascular Modeling Toolkit* (*vmtk*) (Izzo et al., 2018), was employed for the segmentation of the TA

lumen from its ascending segment to the distal section, at the level of the coeliac tripod, to comprise the first four thoracic *landing zones* of the Ishimaru's map (Ishimaru, 2004). Then, by means of the *Paraview* (Ahrens et al., 2005) filter *Ruler*, the left common carotid artery (LCCA) diameter at its origin and the distance between the onset of the brachiocephalic artery (BCA) and the top of the arch were measured. As the latter was more than two times greater than the diameter of the carotid, the aortic arch was classified as Type III according to the Aortic Arch Classification.

The following step consisted in virtually creating the other two arch types, namely Types I and II, varying the arch curvature, using *Autodesk Meshmixer* (Inc., 2019). The main available functions adopted for this purpose were *Transform*, for tilting in space the aortic arch, *Erase & Fill* and *Discard*, for progressively smoothing the modified surface; moreover, *Remesh* tool was used to keep a high-quality surface mesh, that is, with fine triangulation, to avoid sharp edges while changing aortic curvature.

After checking that arch types had been reproduced properly, pathological aortic configurations were developed by exploiting *Boolean Union* of spheres in *Meshmixer*, and subsequently smoothing the bulging surface to create fusiform aneurysms with a maximum diameter of 60 mm, that is the critical value at which the incidence of aneurysm rupture, dissection or patient death reaches the maximum level (Elefteriades & Botta, 2009). For each of the three arch models, the position of the virtually added aneurysmal dilation was varied distally along the descending portion of the vessel, thus leading to the creation of the nine DTAA cases.

Figure 1*A* shows the 12 configurations created following the aforementioned procedure. In what follows, these will be referred to as X–Y, where X = H, P, C, D indicates the location of the aneurysm (Healthy, Proximal, Central and Distal), whereas Y = I, II, III based on the arch type.

Patient-specific geometries. Regarding the patient-specific configurations, we selected three patients (PT-09, PT-40 and PT-71) from Fondazione IRCCS Ca' Granda Ospedale Maggiore – Policlinico di Milano dataset, who had undergone preoperative CTA scanning for TEVAR procedure planning. The acquisitions of CTA images were performed with a Siemens Somatom Definition Flash scanner (Siemens Healthineers, Forchheim, Germany) with the following acquisition parameters: slice thickness of 3.0 mm, reconstruction matrix of 512 × 512 pixels and in-plane resolution of 0.629 mm × 0.629 mm. The patients were selected because they had a TA similar to some of the idealized configurations in terms of arch type and aortic tortuosity. In particular, PT-09, PT-40 and PT-71 presented a central, distal and proximal DTAA, respectively. Vascular surgeons classified the aortic arch as Type III for PT-09, as Type I for PT-40 and as Type II for PT-71. The reconstruction of the patients' TA lumen was performed

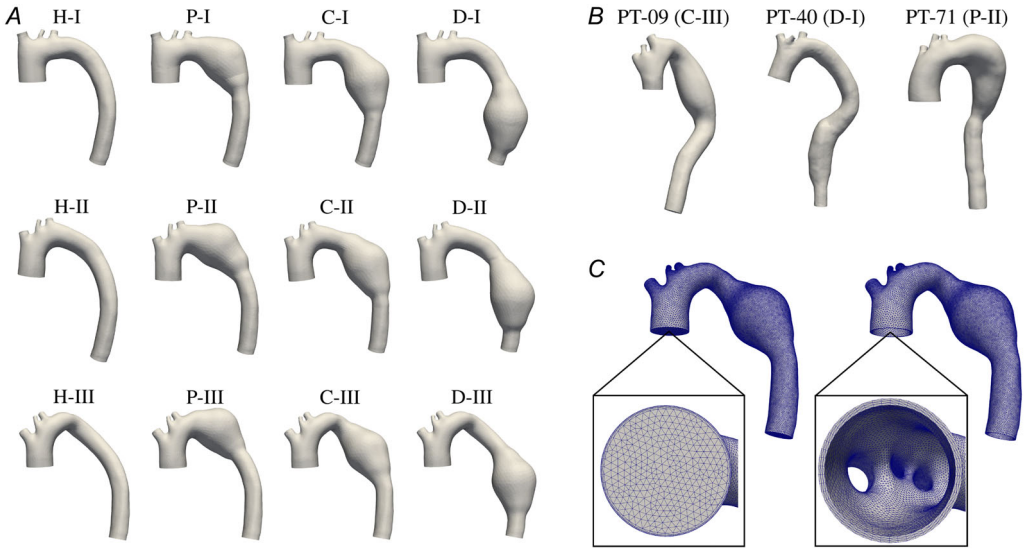

Figure 1.
(A) Twelve virtual scenarios. Every virtual geometry is named by considering the location of aneurysm (H for healthy, P for proximal, C for central, D for distal) and arch type (I for Type I, II for Type II, III for Type III). *(B)* Three patient-specific configurations. PT-09: Type III with central aneurysm. PT-40: Type I with distal aneurysm. PT-71: Type II with proximal aneurysm. In the brackets, we report the corresponding virtual scenario. *(C)* Left: tetrahedral fluid mesh for C-III configuration (chosen here as representative). The black box shows a zoom on the three-layered boundary layer. Right: tetrahedral solid mesh for C-III configuration (chosen here as representative). The black box shows a zoom on the three mesh layers.

by segmenting their preoperative CTA scans using *vmtk* (as explained in 'Virtual geometries' section). The three patient-specific geometries are shown in Fig. 1*B*.

Computational meshes. For all the 12 virtual surfaces and the three patient-specific configurations, the computational fluid meshes were generated exploiting *vmtk*. Specifically, the dimension of the meshes' tetrahedral cells was defined as radius-dependent, so that the grid element size decreased as the diameter of the vessel diminished, except for the aneurysm area, where a constant value equal to 1.5 mm was set. Moreover, close to the vessel wall, we considered a *boundary layer* (BL) composed by three sub-layers with a total thickness of 0.5 mm for the supraortics and 1.0 mm for the rest of the domain. Fig. 1*C* (on the left) shows the generated fluid mesh.

As the available CTA images did not allow us to detect the aortic wall, we created the meshes for the solid problem by extruding outward the fluid mesh's external surface and selecting a wall thickness equal to 10% of the lumen radius for the healthy vessel and equal to 1.5 mm (Van Puyvelde et al., 2016) for the aneurysmatic wall. In any case, a three-layered solid mesh was generated. Figure 1*C* (on the right) shows the generated solid mesh.

Mathematical modelling

In the present study, blood was assumed to be a Newtonian, homogeneous and incompressible fluid, with a density of 1060 kg/m^3 and viscosity of $3.5 \cdot 10^{-3}$ Pa s; accordingly, its behaviour was mathematically modelled with the Navier–Stokes equations written in the *Arbitrary Lagrangian–Eulerian* (ALE) formulation (Van de Vosse et al., 2003), where we used finite elasticity as lifting operator to recover the fluid domain configuration (Johnson & Tezduyar, 1994; Shamanskiy & Simeon, 2021). In case of pathological conditions, included DTAAs, transition to turbulence may be present and should be accounted for in the numerical simulations (Tan et al., 2009). The σ-model *Large Eddy Simulation* (LES) turbulence model (Nicoud et al., 2011; Vergara et al., 2017) was used, as it is suitable for enclosed domains, such as vessels and ventricles.

Regarding the structure, the aortic wall was considered nearly incompressible and linearly elastic (Gao et al., 2006). The density of the aortic wall was set to 1000 kg/m^3, while the Poisson's ratio was set to 0.45. As the wall stiffness is a subject-specific parameter, a universal value does not exist. In this work, the Young's modulus of the healthy part of the TA was set equal to 0.8 MPa, consistent with the literature (Lantz et al., 2011) while, as the aorta tends to stiffen when increasing its diameter (Vorp et al., 2003), the elastic modulus of the aneurysmatic wall was set equal to 1.2 MPa (Azadani et al., 2013). Thus the aortic wall dynamics was formulated by means of the linear elasticity (Hooke's law) written in the *Lagrangian configuration* (Donea et al., 2004), accounting for two different Young's moduli for the healthy and the diseased parts.

Finally the fluid and structure sub-problems were coupled at their interface surface through the *kinematic condition*, which provided the perfect adhesion between the fluid and structure particles; the *dynamic condition*, which prescribed the equilibrium between the fluid and structure forces; the *geometric condition*, which guaranteed perfect adherence between the fluid and structure domains (Quarteroni et al., 2017).

Because each computational simulation was performed on a specific region of interest, which was a limited part of the whole cardiovascular system, the regions excluded from the model had to be considered by exploiting suitable boundary conditions (BCs). Regarding the fluid problem, at the ascending TA (ATA) inlet, a physiological time-dependent pressure-wave ranging between 70 and 120 mmHg of 0.735 s period was imposed (Fig. 2*A*) (Alastruey et al., 2012). Moreover, to avoid the phenomenon of spurious reflections that may be caused by the artificial truncation of the computational domain, at each supraortics outlet (i.e. BCA, LCCA and left subclavian artery (LSA)), a proper absorbing boundary condition consisting of one resistance was prescribed (Nobile & Vergara, 2008) (Fig. 2*B* on the left). Finally at DTA outlet, a 3-Element Windkessel Model (3-EWM) was imposed, as it provided a dynamic relationship between pressure and flow rate accounting for the downstream circulation (Westerhof et al., 2009) (Fig. 2*B* on the left).

Regarding the computational solid domain, at each inlet and outlet, a null displacement condition was prescribed, whereas on the external surface, a Robin condition (Moireau et al., 2012) with springs of stiffness K_{ext} was supplied by a dissipative element of capacity C_{ext} (Regazzoni et al., 2022) modelling the constraint exerted by the surrounding tissue (e.g. the spinal column) on the vessel's movements (Fig. 2*B* on the right).

Numerical approximation and setting of the numerical simulations

Regarding the numerical approximation of the FSI problem, for the time discretization, we imposed a time-step $\Delta t = 5 \cdot 10^{-4}$ s, and we considered the semi-implicit backward differentiation formula of second-order (BDF2) for the fluid sub-problem, whereas first-order BDF1 for the structure problem. At time t^{n+1}, in the σ-LES model, we computed the turbulent viscosity using the two-order extrapolation of fluid velocity from the previous time steps (Nicoud et al., 2011). Moreover both the absorbing and 3-EWM BCs were coupled

explicitly to the Navier–Stokes equations, that is, the boundary pressure at time t^{n+1} was computed exploiting the flow rate calculated from the previous time step t^n (Pozzi et al., 2021). At each time step t^{n+1}, we solved first the lifting problem with boundary displacement obtained from the structure problem at time t^n; then, once the new fluid domain had been computed, the FSI problem was solved monolithically by using GMRES pre-conditioned by means of a block pre-conditioner (see Bucelli et al. (2023)).

For each configuration reported in Fig. 1, the simulation was performed over 10 cardiac cycles of which we discarded the first 3 to allow the stabilization of flow velocity and pressure fields. Indeed, after four cycles, the numerical results reached a regime configuration with, however, fluctuations among heartbeats (HBs) due to transition to turbulence.

All the numerical simulations were performed using life^x (Africa, 2022; Africa et al., 2024): a high-performance library for the finite element simulations of multi-physics, multi-scale and multi-domain problems, developed at the MOX, Dipartimento di Matematica, with the collaboration of LaBS, Dipartimento di Chimica, Materiali e Ingegneria Chimica, both at Politecnico di Milano.

As a preliminary step before running the final simulations, a calibration of the BC parameters was necessary. In particular, for all the parameters, a literature formula was used to propose an initial guess. Specifically, for the supraortics, the absorbing resistances R_{BCA}, R_{LCCA} and R_{LSA} were computed based on geometric and mechanical quantities, using the formula reported by Nobile et al. (2013):

$$R_{absorbing} = \sqrt{\frac{\rho E H_s}{2(1-\nu^2)R^2}}\frac{1}{A_0^{3/4}}, \tag{1}$$

where ρ is the blood density, E is the Young's modulus of TA, H_s is the aortic wall thickness, ν is the Poisson ratio, R is the outlet radius and A_0 is the outlet area in the undeformed configuration. For the calibration of the 3-EWM parameters, the proximal resistance R_1 was set as the one obtained in the case of a resistance absorbing boundary condition; the distal resistance R_2 was set according to Romarowski et al. (2018), basically subtracting R_1 to a total peripheral resistance, computed as the ratio between the time-averaged inlet pressure and flow rate:

$$R_2 = \frac{\frac{1}{T}\int_0^T P(t)}{\frac{1}{T}\int_0^T Q(t)} - R_1. \tag{2}$$

Instead, the compliance C was computed following the formula reported by Alastruey et al. (2012):

$$C = \frac{Q_{max} - Q_{min}}{P_s - P_d}\Delta t, \tag{3}$$

where Q_{min} and Q_{max} are the minimum and maximum blood flow rates in a cardiac cycle at the inlet, P_s and P_d are the systolic and diastolic pressure (all these values were taken from Alastruey et al. (2012)) and Δt is the distance in time between Q_{min} and Q_{max}. The downstream pressure P_{ext} (see Fig. 2*B* on the left) was set to 70 mmHg in accordance with the values estimated by Alastruey et al. (2016). The initial guesses obtained through the formulas reported above were subsequently tuned, performing several simulations using the H-I configuration, to ensure that approximately 75% of the cardiac output entering in ATA exited through DTA (Coats, 1990). The two Robin parameters in the external structure BC were guessed starting from the values reported in Moireau et al. (2012), and then calibrated to guarantee a physio-

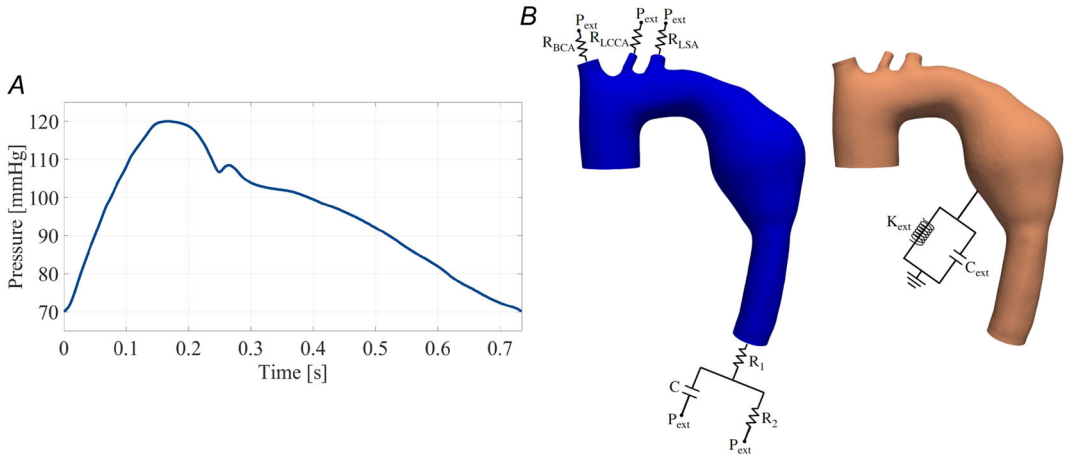

Figure 2. Boundary conditions prescribed for all the configurations (i.e. virtual and patient-specific)
(*A*) Time-dependent inlet pressure waveform adapted from Alastruey et al. (2012). (*B*) Left: Absorbing and Windkessel boundary conditions prescribed at the outlets of the computational fluid domain. Right: Robin boundary condition prescribed on the external surface of the computational structure domain.

Table 1. Values of the calibrated parameters imposed in the outlet boundary conditions for the supraortic branches (BCA, LCCA, LSA) and for DTA

R_{BCA} [kg/(s m^4)]	$1.50 \cdot 10^8$
R_{LCCA} [kg/(s m^4)]	$7.50 \cdot 10^8$
R_{LSA} [kg/(s m^4)]	$5.50 \cdot 10^8$
R_1 [kg/(s m^4)]	$2.30 \cdot 10^7$
R_2 [kg/(s m^4)]	$6.08 \cdot 10^7$
C [(m^4 s^2/kg]	$8.00 \cdot 10^{-7}$
K_{ext} [Pa/m]	$1.50 \cdot 10^6$
C_{ext} [(Pa s)/m]	$4 \cdot 10^5$

Table 2. Boundary layer sensitivity analysis results

T_1^{aorta} [mm]	τ_{max}^{aorta} [Pa]	y_{aorta}^+ [–]	$T_1^{sup.}$ [mm]	$\tau_{max}^{sup.}$ [Pa]	$y_{sup.}^+$ [–]
0.14	13.19	1.11	0.071	17.13	0.44

logical cross-sectional area variation of about 10% during a cardiac cycle (Van Prehn et al., 2009). Table 1 shows the final calibrated values.

Mesh sensitivity analysis

To allow reliable elaboration of WSS values obtained by the numerical simulations, the blood flow close to the wall has to be accurately captured, and hence, the first layer of the fluid mesh grid must be sufficiently close to the wall. This distance from the wall is represented as a non-dimensionless distance y^+ which, according to the turbulent BL sub-layer coordinates (Wilcox et al., 1998), should be less than 2 to guarantee the correct WSS detection. Therefore, once we had chosen the thickness of the first BL sub-layer T_1, we computed y^+ exploiting the formula (Febina et al., 2018):

$$y^+ = \frac{T_1 u_t}{\mu/\rho}, \tag{4}$$

where $u_t = \sqrt{\frac{\tau_{max}}{\rho}}$ is the friction velocity, in which τ_{max} is the maximum WSS value during a cardiac cycle. Because the total BL thickness was different for TA and the supra-ortics (see 'Computational meshes' section 2.1.3), and consequently also the thickness of the first sub-layer, we ensured that y^+ was less than 2 for both parts of the geometry (Table 2).

Subsequently a sequence of three finite element meshes of increasing density was used to perform a mesh sensitivity analysis to establish the most suitable fluid and solid mesh grid size, which ensured the correct balance between accuracy of the results and runtime of the simulations, and to avoid grid resolution errors. Thus each simulation was run on three different couple H-I fluid and solid meshes (i.e. M1, M2 and M3) with a grid size h_{fluid} and h_{solid} progressively finer. The simulations were run for two HBs with the same inlet pressure-wave (Fig. 2*A*), and only the results of the second cycle were considered. The results were declared mesh independent when the DTA outlet systolic peak flow rate (Q_{peak}), peak WSS (τ_{peak}) and peak wall displacement (d_{peak}) between successive meshes satisfied the following relation:

$$\Delta_{i-1,i} = \left| \frac{Q_i - Q_{i-1}}{Q_{i-1}} \right| \leq \epsilon_{i-1,i}, \tag{5}$$

where Q is the quantity of interest evaluated for the coarser $(i-1)$-th and the finer i-th mesh, and $\epsilon_{i-1,i}$ is the tolerance computed as follows:

$$\epsilon_{i-1,i} = M(Q) cos\left(\frac{\pi}{2} r_{i-1,i}\right), \tag{6}$$

where $r_{i-1,i} = \frac{h_i}{h_{i-1}}$ is the refinement ratio between the coarser $(i-1)$-th and the finer i-th mesh size, and $M(Q)$ is an acceptable clinical error, prescribed according to the accuracy associated with a specific diagnostic technique (e.g. echo colour Doppler accuracy in measuring blood flow velocity). Table 3 summarizes the size, the number of cells and the quantities of interest for all the meshes considered.

Table 3. Grid size, number of cells and computed quantities of interest among the three meshes

Mesh	h_{fluid} [mm]	h_{solid} [mm]	N_{fluid} [–]	N_{solid} [–]	Q_{peak} [ml/s]	τ_{peak} [Pa]	d_{peak} [mm]
M1	1.57	1.57	957,634	283,431	271.82	11.85	6.10
M2	1.30	1.30	1,307,670	336,568	273.25	13.19	6.11
M3	1.04	1.04	2,004,246	553,546	273.51	13.60	6.15

h_{fluid}: average size of the fluid mesh grid, h_{solid}: average size of the solid mesh grid, N_{fluid}: number of cells of the fluid mesh, N_{solid}: number of cells of the solid mesh, Q_{peak}: DTA outlet blood flow rate at the systolic peak, τ_{peak}: WSS at the systolic peak, d_{peak}: wall displacement at the systolic peak.

Defining the tolerance $\epsilon_{i-1,i}$ as prescribed by eqn (6), two limit conditions may occur:

(1) $r_{i-1,i} = 1$ and $\epsilon_{i-1,i} = 0$: this corresponds to a condition in which no mesh refinement is carried out, and thus the tolerance must be equal to zero as the quantities of interest computed in two consecutive meshes must be the same;
(2) $r_{i-1,i} \to 0$ and $\epsilon_{i-1,i} \to M(Q)$: this corresponds to a condition in which an excessive refinement is carried out and, for its definition, the refinement

Table 4. Mesh sensitivity analysis based on the computed quantity of interest, that is, DTA systolic peak blood flow rate (Q_{peak}), peak WSS (τ_{peak}) and peak wall displacement (d_{peak})

	$r^{fluid}_{i-1,i}$ [%]	$r^{solid}_{i-1,i}$ [%]	Q_{peak}		τ_{peak}		d_{peak}	
			$\epsilon_{i-1,i}$	$\Delta_{i-1,i}$	$\epsilon_{i-1,i}$	$\Delta_{i-1,i}$	$\epsilon_{i-1,i}$	$\Delta_{i-1,i}$
M1–M2	82.78	82.77	1.34	0.53	2.67	11.31	1.34	0.16
M2–M3	79.81	79.88	1.56	0.09	3.12	3.11	1.55	0.65

$r^{fluid}_{i-1,i}$ and $r^{solid}_{i-1,i}$ denote the refinement ratio between the coarser ($i-1$-)th and the finer i-th mesh. The specific tolerances $\epsilon_{i-1,i}$ and the relative difference of each quantity $\Delta_{i-1,i}$ between two consecutive meshes are computed following eqns (6) and (5), respectively. The acceptable error $M(Q)$ is set to 5% for Q_{peak} and d_{peak}, while it is set to 10% for τ_{peak}. All the reported quantities are percentages and $i = 1,2,3$.

ratio would tend to zero and thus the tolerance must tend to $M(Q)$, that is, the error that is considered acceptable in clinical practice which therefore could be considered as the error associated with the real solution.

In this way, we were able to correlate the tolerance $\epsilon_{i-1,i}$ with the refinement ratio $r_{i-1,i}$, which in turn allowed us to consider larger $\epsilon_{i-1,i}$ (if associated with a sufficiently great degree of refinement), instead of using a fixed tolerance value, which sometimes could be unnecessarily small.

Table 4 shows the results of the mesh sensitivity analysis, reporting the relative difference of a certain quantity Q between two consecutive meshes and the prescribed tolerances. The latter were found following eqn (6), considering $M(Q) = 5\%$ for Q_{peak} and d_{peak} (Powell et al., 2000) and $M(Q) = 10\%$ for τ_{peak} (Pantos et al., 2007). In Table 4, cells coloured in green show that the relative difference of a certain Q is less than the tolerance, vice versa cells coloured in red show that the difference is greater than the tolerance. Accordingly, the most suitable choice was M2, as its grid size was sufficiently fine to ensure that the differences in quantities between M2 and M3 were below the imposed tolerance for both fluid and solid meshes, while it almost halved the computational time. In fact, while the total time required to simulate one HB with M1 was 4 h, M2 needed approximately 6 h against 14 h required for M3.

Quantities of interest

Preoperative analysis. To comprehensively observe and describe the hemodynamics and wall motion in all the configurations, we quantitatively evaluated the blood pressure and velocity and structural displacement computed by the numerical simulations. Specifically we computed the *ensemble* values of such quantities, that is, the average calculated, at each time and at each point of the domain, over the seven HBs. Moreover we estimated the following quantities:

- Standard deviation (SD) at each time and space of the blood velocity with respect to its ensemble value. This allowed us to quantify and localize the regions with considerable large velocity fluctuations, which were characterized by marked transition to turbulence (Vergara et al., 2017).
- (Ensemble) Oscillatory shear index (OSI): a dimensionless descriptor which allows the identification of zones of the artery wall subjected to large directional variations of the WSS vector during a cardiac cycle, computed as follows (Ku et al., 1985):

$$OSI(\mathbf{x}) = \frac{1}{2}\left(1 - \frac{\left|\int_0^T \mathbf{WSS}\, dt\right|}{\int_0^T |\mathbf{WSS}|\, dt}\right), \tag{7}$$

where **WSS** is the (ensemble) WSS vector and T is the cardiac cycle duration. In aneurysms, high values of OSI favour the development of atherosclerosis, inflammation of the artery and internal thickening of the arterial wall (Mutlu et al., 2023).
- (Ensemble) von Mises stress (VMS): a structural quantity that allows for an evaluation of the stresses a sample material is subjected to, to establish the response of the former to a certain complex loading condition. VMS is commonly used as a criterion for material failure and to predict the effect of the hemodynamics on the internal wall of aneurysms, associating high value of VMS to the possibility of aneurysm rupture (Tan et al., 2009). Exploiting the assumption of linear elasticity introduced for the aortic mechanics modelling (see 'Mathematical modelling' section, we were able to compute VMS, σ_{VM}, with the formula:

$$\sigma_{VM}(t, \mathbf{x}) = \sqrt{\frac{(\sigma_I - \sigma_{II})^2 + (\sigma_{II} - \sigma_{III})^2 + (\sigma_I - \sigma_{III})^2}{2}}, \tag{8}$$

where σ_i, with $i = I, II, III$, are the principal stresses of the Cauchy stress tensor in the ith direction related to the Hook's law.

- (Ensemble) *drag forces*: these are the forces (i.e. pressure and WSS) exerted by the blood on the vessel wall. For each of the geometries considered in this study (see Fig. 1), we considered a sub-division, coming from the clinical practice, useful to assess how the state of stress along the vessel was distributed. Specifically TA was sub-divided into landing zones according to the Modified Arch Landing Areas Nomenclature (MALAN) classification (Marrocco-Trischitta et al., 2017) (see Fig. 3*A*), which merges Ishimaru's map (Ishimaru, 2004) with the Aortic Arch Classification (Madhwal et al., 2008). We were interested in considering the (vectorial) average of drag forces onto each landing zone surface *LZ* (refer to Fig. 3*B*) (Marrocco-Trischitta et al., 2018):

$$\overline{\mathbf{DF}}(t) = \int_{LZ} p\mathbf{n}\, d\mathbf{x} + \int_{LZ} \mathbf{WSS}\, d\mathbf{x}, \qquad (9)$$

  where $\mathbf{n}$ is the outward normal evaluated at the wall. Notice that, $\overline{\mathbf{DF}}$ is a variable which, at each time t, assumes different constant values over the different landing zones. With $|\overline{\mathbf{DF}}|$, we will indicate its magnitude.
- (Ensemble) $DF_{\parallel}$ and (ensemble) $DF_{\perp}$: parallel (tangential) and normal (perpendicular) main components of $\overline{\mathbf{DF}}$ normalized over the area A of each landing zone:

$$DF_{\perp}(t) = \frac{\overline{\mathbf{DF}} \cdot \mathbf{n}}{A}, \qquad DF_{\parallel}(t) = \left| \frac{\overline{\mathbf{DF}}}{A} - DF_{\perp}\mathbf{n} \right|. \qquad (10)$$

  $DF_{\parallel}$ is aligned with the aortic centreline, while $DF_{\perp}$ acts orthogonally to the wall of the vessel, in the outward direction (Fig. 3*B*).

Towards a preliminary TEVAR analysis. In what follows, we wanted to propose an index in view of the possible application of our preoperative analysis to the case of TEVAR procedure. In this context the introduction of $DF_{\parallel}$ and $DF_{\perp}$ aimed also to provide additional useful information to clinicians who were interested in predicting unwanted TEVAR late complications, especially the endograft migration. In view of preventing the latter risk, we considered the following four possible mechanisms:

(i) It would be better to avoid landing zones in which $DF_{\parallel}$ resulted to be noticeably high, as it could promote the migration of the stent-graft, which would be subjected to a significant force in the direction of the flow ($\sim DF_{\parallel}$).
(ii) It would be better to avoid landing zones where $DF_{\parallel}$ (independently of its actual value) resulted to be predominant over $DF_{\perp}$ (Domanin et al., 2021) and, for this reason, we considered important the ratio $DF_{\parallel}/DF_{\perp}$ as, for the same $DF_{\parallel}$, the condition with larger $DF_{\perp}$ was to be preferred, as it ensured that the stent-graft would be subjected to a sufficient radial force to guarantee its safe anchoring ($\sim DF_{\parallel}/DF_{\perp}$).
(iii) We speculated that too high values of $DF_{\perp}$ could be dangerous, as they could cause an excessive vessel dilatation, leading to the stent-graft detachment and, at the level of the aortic arch, to *endoleak* formation, which could be a further source of stent-graft migration (Thomas & Sanchez, 2009) ($\sim \sqrt{DF_{\perp}}$).
(iv) We considered as unfavourable the situation in which the presence of the aneurysm caused a considerable increase in the parallel component with respect to the healthy condition, used as reference for a normal scenario ($\sim DF_{\parallel}/\sqrt{DF_{\parallel}^{H}}$).

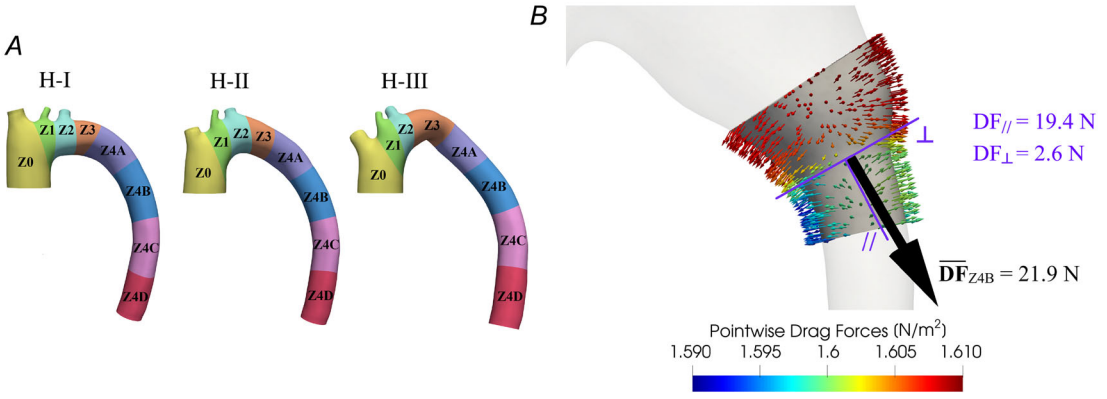

Figure 3.
(*A*) Landing zones map for each aortic arch type according to the MALAN classification. (*B*) Example of the evaluation of $DF_{\parallel}$ and $DF_{\perp}$ in landing zone Z4B for P-II configuration. Coloured arrows: pointwise (ensemble) drag forces. Black arrow: average drag force $\overline{\mathbf{DF}}$ at the systolic peak. The direction $\parallel$ tangent to the centreline and its outward perpendicular direction $\perp$, used to determine the $DF_{\parallel}$ and $DF_{\perp}$ components, respectively, are shown in purple.

To take into account all the dangerous conditions mentioned above and to provide valuable insights about which landing zones would be the safest in view of the stent-graft anchoring, we proposed the following synthetic index β (*risk factor*), which was computed for each landing zone as follows:

$$\beta(t) = \frac{\left(DF_{\parallel}\right)^3}{10^6\sqrt{DF_{\perp} \times DF_{\parallel}^H}}, \tag{11}$$

where $DF_{\parallel}^H$ is the parallel component of the average drag forces in the healthy configuration.

Results: virtual configurations

In this section, we report the results of the numerical simulations performed in all the virtual configurations. First, we report the results in terms of average quantities for the healthy and for one representative DTAA ideal case ('Average quantities' section); then, we report the 3D results of the simulations conducted in the virtual cases ('Comparison of hemodynamics and structural stresses' section), with a focus on drag forces ('Analysis of drag forces' section).

Average quantities

In Fig. 4, we report the average blood flow rate and the cross-sectional area variation within one HB for H-I and C-I scenarios, selected here as representatives for the DTAA cases.

First, we notice that our simulations are able to satisfy for the healthy scenario the two criteria used for the outflow BC calibration (75% of inflow reaches the DTA outlet and area variation in time of about 10%, see 'Numerical approximation and setting of the numerical simulations' section). Indeed we have a plausible average-in-time inlet blood flow rate of 6.6 L/min (Critchley & Critchley, 1999), against 5.1 L/min at the DTA outlet, corresponding to 77% of the inflow, while the remaining 23% goes to the neck vessels, in accordance with literature data (Coats, 1990). This corresponds to the plots in time reported in continuous lines in Fig. 4*A*. The negative flow at the end of the cycle (about 6% of the ATA flow rate) is plausibly the blood flowing to the coronary arteries supplying the myocardium. As regards the second criterion, we notice from Fig. 4*B* that, for the H-I configuration, the maximum area variation is 12.4%, in good accordance with the literature values (Van Prehn et al., 2009).

Second, in what follows, we discuss the differences obtained between the results of H-I and C-I scenarios. Regarding the blood flow rate, in the diseased scenario, we have the same average-in-time value than in the healthy case (6.6 L/min), as a consequence of the same inlet pressure and outlet resistances and compliance in the two cases. However from Fig. 4*A* we notice that, in C-I scenario, the flow rate at the systolic peak is higher (17% more) than in the healthy configuration. Instead, for the area variation, we notice percentage values that are almost half (6.6%) of the healthy scenario, in accordance with the increased Young's modulus in the aneurysm of C-I configuration.

Comparison of hemodynamics and structural stresses

In what follows, we report 3D maps of the ensemble quantities of interest obtained in the numerical simulations, such as pressure and velocity fields, velocity SD for turbulence quantification, OSI and VMSs, with the aim of comparing the different hemodynamic answers of the virtual DTAA scenarios described in the previous section.

Pressure and velocity fields. Figure 5*A* shows the ensemble blood pressure over seven HBs at the systolic peak for all the virtual configurations. We observe that while H-I and H-II scenarios have nearly the same trend, in H-III, a region of relative low pressure is clearly visible immediately after the supraortics, where the curvature of DTA is maximum (highlighted by the black box in Fig. 5*A*). Regarding the diseased scenarios, the pressure within the whole aneurysm is uniformly higher than the

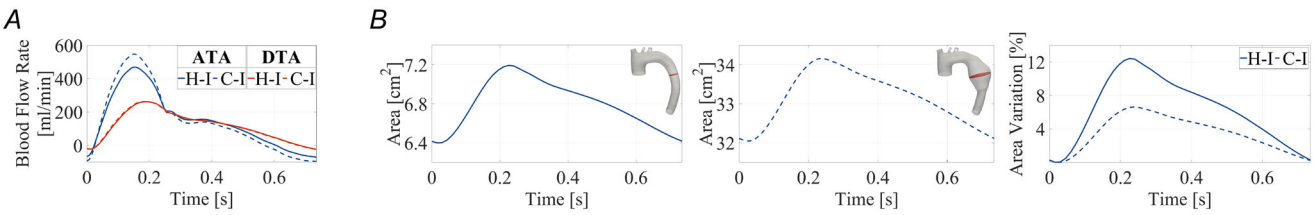

Figure 4.
(*A*) Blood flow rates at the inlet of ATA and at the outlet of DTA during one cardiac cycle for H-I and C-I configurations. (*B*) From left to right: cross-sectional area over time in H-I configuration; cross-sectional area over time in C-I configuration; percentage variation of cross-sectional area in both H-I and C-I configurations. The boxes in the top-right corner highlight in red the cross-section considered.

values found in the other parts of the geometry, and there is also a sudden increase and decrease in pressure values at the proximal and distal necks, respectively (Fig. 5*B*). These findings are in good agreement with what was reported by Campobasso et al. (2018), who proved that an increase in the aortic stiffness could cause an intensification of pressure values in ascending TAAs. The blood pressure is particularly high in C-I, C-II, D-I and D-II configurations, in contrast to the other scenarios, for example, C-III and D-III, where again low pressure values are observed in the region of maximum DTA curvature.

In Fig. 6*A*, we show the ensemble velocity magnitude over seven HBs at the systolic peak for all the configurations considered. It is possible to notice that, in the healthy tracts, the blood flow is very stable, characterized by smooth and almost parallel streamlines. On the contrary the presence of the aneurysmal sac causes the flow to be slightly more chaotic, with re-circulation regions at the proximal aneurysm neck in all the cases and with another vortical structure, adjacent to the inner side wall within the aneurysm, in C-III (black box in Fig. 6*A*). Besides, while the ensemble velocity magnitude considerably decreases within the aneurysm, it increases in the regions just upstream and downstream of the bulging if compared to the healthy cases, particularly in D-II, C-III and D-III configurations. In particular in the region not directly affected by the pathology blood velocity records values up to 0.70 m/s, whereas in the aneurysmal sac, it decreases greatly, reaching values between 0.10 and 0.30 m/s, in good accordance with what was found by Silva et al. (2023).

In Fig. 6*B*, we consider the diastolic phase observing that, in the aneurysm, blood velocity remains higher than in the healthy cases with large vortices (black box in Fig. 6*B*), which are more evident in P-II, C-II, D-II, P-III and C-III configurations. The vortical structures forming within the aneurysm show velocity values ranging from 0.30 and 0.40 m/s, consistent with what was reported by Silva et al. (2023).

Transition to turbulence. In Fig. 7, we report the SD of the velocity magnitude over seven HBs for all the virtual configurations considering three time instants: early systole (Fig. 7*A*), late systole (Fig. 7*B*) and late diastole (Fig. 7*C*). Large SD values in a region represent high-velocity fluctuations among HBs in that region. This is an index of transition to turbulence (Vergara et al., 2017).

At all the time instants considered, in H-I and H-II configurations, the velocity fields are almost stable with little fluctuations, in contrast with H-III case where, in the descending portion, velocity fluctuations are more

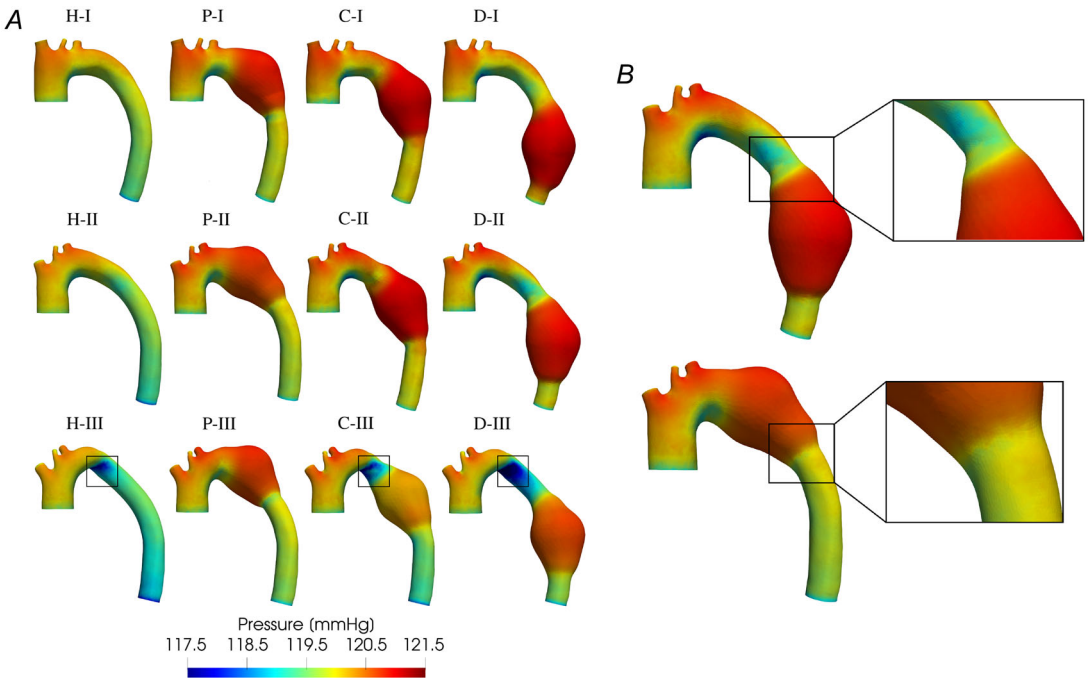

Figure 5.
(*A*) Ensemble blood pressure at the systolic peak(t = 0.165 s) in all the virtual configurations. Black boxes highlight the low pressure region in the inner curvature of the arch of the Type III configurations. (*B*) Top: sudden increase in pressure value at the proximal aneurysm neck in D-II configuration (chosen as a representative diseased case). Bottom: sudden decrease in pressure value at the distal aneurysm neck in P-II configuration (chosen as a representative diseased case).

visible. Regarding the aneurysmatic configurations, Fig. 7 shows larger values of ensemble velocity SD for all the diseased scenarios at each time instant, especially during the deceleration phase of the cycle, where SD reaches values even up to about 25% of the maximum ensemble velocity. Specifically, the highest SD values are observed in the aneurysmal sac, where, due to the sudden change of morphology, the fluctuations are maximum. Among the DTAA cases, C-III seems to be the one that most favours transition to turbulence.

Oscillatory shear index and von Mises stresses. In Fig. 8*A*, we compare the ensemble OSI for all the pathological configurations with their healthy counterparts. We notice that in all the diseased scenarios, OSI assumes significantly high values (>0.4) largely on the lateral walls of the aneurysmal sac, in good accordance with what was found by Tan et al. (2009), except for C-III and D-III. Moreover we observe that in P and C configurations, in correspondence of the proximal and distal aneurysm necks, there are both regions of very low (<0.1) and very high OSI values. On the contrary, in D configurations, the proximal aneurysm neck is only characterized by high OSI, whereas the distal neck shows only low values. In all the diseased cases, on the superior wall of the aneurysm, in correspondence of the dome, there is a region of great OSI, which is followed further downstream by an area with low OSI values. The other part of the geometries not affected by the disease maintains nearly the same OSI values of the healthy scenarios: high OSI values are observed in ATA, at supra-aortics bifurcations and on the lesser curvature side of the arch, consistently with Numata et al. (2016).

In Fig. 8*B*, we report the ensemble VMSs at the systolic peak on the aortic wall for all the virtual configurations. In the pathological cases, a clear distinction between the state of stress in the healthy portion of the geometry and in the aneurysm can be seen, due to their different Young's moduli. In particular, in the aneurysm, there is a VMS increase up to 33% with respect to the healthy cases. The proximal and distal aneurysm necks present regions characterized by the greatest VMS increase (almost 160 kPa), whereas the area localized at the centre of the aneurysmal sac shows relatively lower values (about 130 kPa). Also Silva et al. (2023) found that maximum VMS did not occur in the larger diameter aneurysm section, but

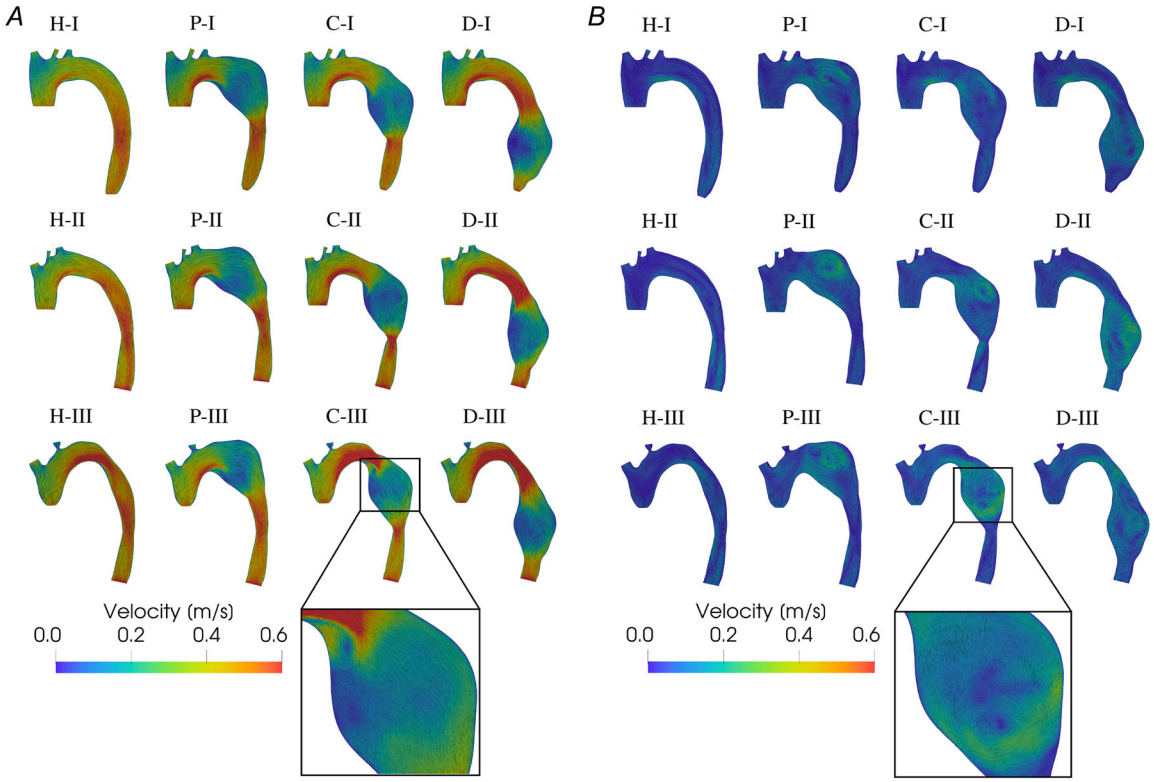

Figure 6.
(A) Ensemble velocity magnitude over seven HBs at the systolic peak (t = 0.165 s) in all the virtual configurations. Black box highlights the two vortices forming at the proximal aneurysm neck and on the inner side wall within the aneurysm in C-III configuration. *(B)* Ensemble velocity magnitude over seven HBs at late diastole (t = 0.645 s) in all the 12 virtual configurations. Black box highlights the vortex forming within the aneurysm in C-III configuration (chosen here as representative).

at the aneurysm neck, reporting an increase in VMS values within TAA from 100 kPa, in the region not afflicted by the pathology, up to 210 kPa.

Analysis of drag forces

In this section, we report the ensemble drag forces results aiming to outline the changes that DTAA may cause on such hemodynamic forces, highlighting the differences between the healthy and the aneurysmatic cases, as well as the differences between each diseased scenario, first in terms of drag force magnitude and then in terms of orientation.

Figure 9 shows the resultant average drag force vectors $\overline{\mathbf{DF}}$ in each landing zone for all the virtual configurations, conventionally applied, for visualization purposes, at the centre point of each landing zone. From now on, in the diseased cases, we refer to those landing zones located in the non-aneurysmatic regions of TA as *standard* landing zones.

In Fig. 9, we observe that, in the healthy configurations, the average drag forces with lower magnitude are located in the landing zones of the descending portion of the vessel (i.e. Z4A, Z4B, Z4C and Z4D), and this behaviour is maintained also in the diseased configurations for the standard landing zones. On the contrary, the presence of the aneurysmal sac causes a considerable $\overline{\mathbf{DF}}$ magnitude increase in the landing zones involved by the pathology. In particular, the areas with the most significant magnitude increase are the landing zones located just upstream and downstream of the sac, while the increase is less notable in the landing zone ubicated in the aneurysm centre. We notice that the highest increase in $|\overline{\mathbf{DF}}|$, with respect to the healthy condition, is attained in D configurations. Moreover, we notice that among all standard landing zones, Z0 is the area with the highest $|\overline{\mathbf{DF}}|$ for Type II

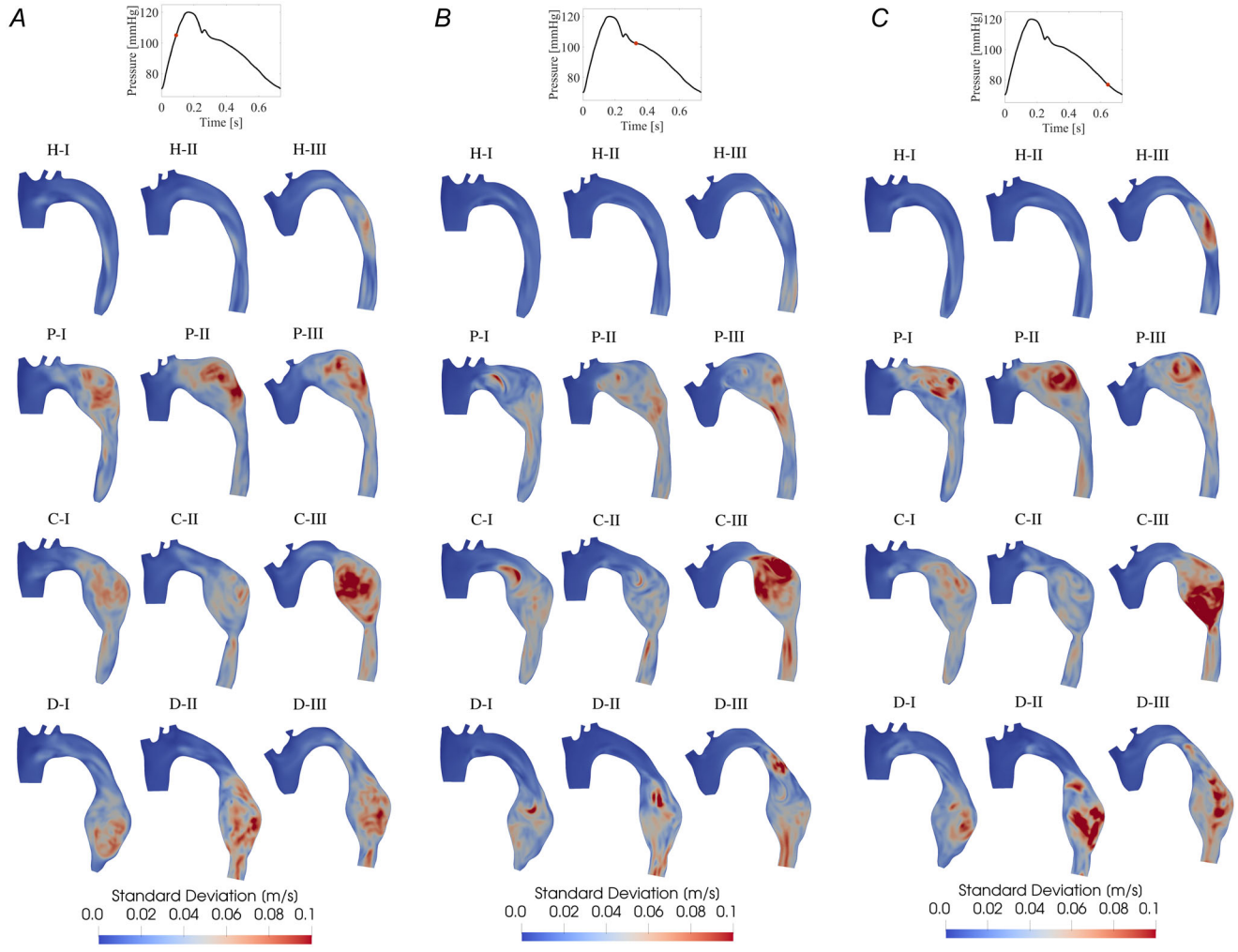

Figure 7. Standard deviation (SD) of the velocity magnitude over seven HBs in all the virtual configurations at three time instants
(*A*) Early systole t = 0.09 s, (*B*) late systole t = 0.33 s and (*C*) late diastole t = 0.645 s.

and III configurations, while it is Z1 for Type I cases. Considering the standard landing zones located at the arch (i.e. Z1, Z2 and Z3), it can be noticed that among the three types of arch, Type III reports the lowest values of $|\overline{\mathbf{DF}}|$ in Z1 and Z3, and the highest values in Z2 (except for P-II).

In Fig. 9, in general, we observe that the presence of the aneurysm causes the orientation of average drag forces to shift gradually towards the vessel centreline direction, especially in the landing zones ubicated at the proximal and distal aneurysm necks. Regardless of the aneurysm ubication, $\overline{\mathbf{DF}}$ is oriented along the cranial and caudal directions (i.e. upwards and downwards) in the landing zones located just upstream and downstream of the aneurysmal sac, respectively. In the aneurysm centre, in P-I scenario, $\overline{\mathbf{DF}}$ is oriented along the cranial direction; in D-I and P-II scenarios, it is mainly directed sideways pointing upward, while in the other configurations, it shifts more downwards. Moreover considering the healthy configurations, in the landing zones situated in the descending part of the vessel, the average drag forces are mainly oriented towards the aortic wall (except for Z4A in H-III), and this behaviour is maintained also in standard landing zones in the aneurysmatic scenarios. In addition, we observe that, in all the healthy and diseased configurations, $\overline{\mathbf{DF}}$ in Z0 maintains approximately the same orientation: sideways and directed towards the heart. Finally, regarding the standard landing zones ubicated at the arch, the aortic curvature increase causes the orientation of $\overline{\mathbf{DF}}$ in Z1 and Z2 to shift gradually upwards, while the opposite happens in Z3.

Analysing more in detail how drag forces are oriented, in Table 5, we report the values of $DF_{\parallel}$ and $DF_{\perp}$,

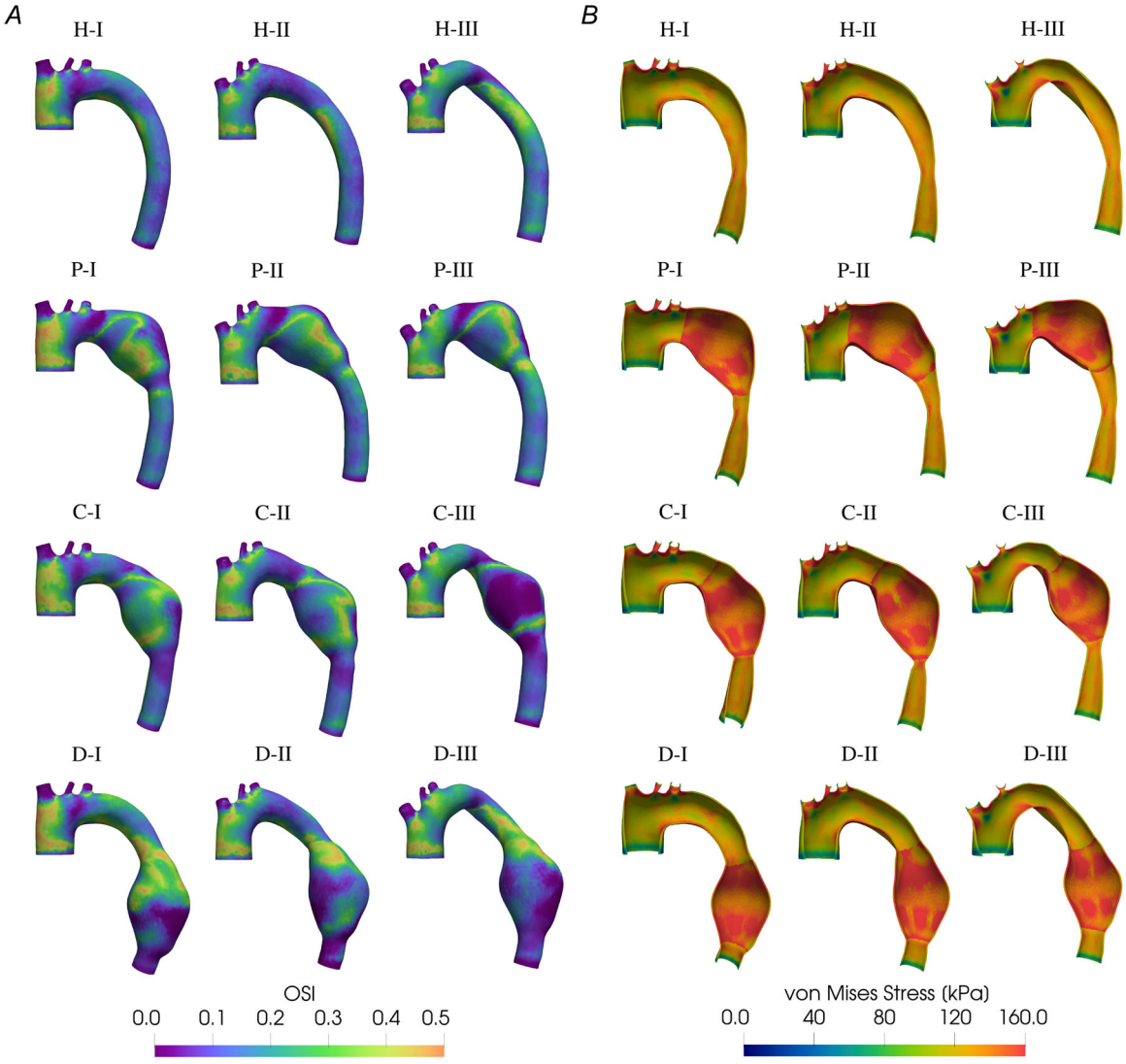

Figure 8.
(*A*) Ensemble oscillatory shear index (OSI) in all the virtual configurations. (*B*) Ensemble von Mises stresses (VMSs) of the aortic wall at the systolic peak (t = 0.165 s) in all the virtual configurations.

expressed in N/m^2, for each landing zone in all the virtual configurations. Regarding the healthy cases we first observe that the greatest drag forces are located in the proximal landing zones with comparable values of $DF_{\parallel}$ and $DF_{\perp}$. Instead the drag force components seem to be elevated in presence of the aneurysm, as highlighted by the grey cells identifying the aneurysmatic landing zones. Specifically, in such regions, landing zones corresponding to the proximal and distal aneurysm necks are always characterized by a $DF_{\parallel}$ larger than $DF_{\perp}$ (except for P-III). Regarding the standard landing zones ubicated at the aortic arch, we observe that the increase in arch curvature increases the number of zones in which $DF_{\parallel}$ is predominant over $DF_{\perp}$. In addition we observe that C-III and D-III exhibit higher values of $DF_{\parallel}$ in almost all the landing zones. In C-II and D-II, in Z2 and Z3, $DF_{\parallel}$ is lesser than $DF_{\perp}$, while the opposite happens in Z1. In C-I and D-I, $DF_{\parallel}$ results to be higher than $DF_{\perp}$ in Z1 and Z2, while it is lower in Z3. In P configurations, $DF_{\parallel}$ is higher than $DF_{\perp}$ both in Z1 and Z2.

In Table 5, we report also the risk factor β evaluated for each landing zone in all the diseased configurations. Consistently with what is observed for $|\overline{\mathbf{DF}}|$ and for $DF_{\parallel}$ and $DF_{\perp}$ values, we notice that, for each configuration, the maximum value of β (red numbers in Table 5) is always attained in correspondence of the aneurysm (grey cells in Table 5). In particular we observe that in six out of nine diseased cases, the highest β is found in the landing zone located in correspondence of the distal aneurysm neck. In addition, the lowest β value, in the regions involved by the pathology, is always encountered in the landing zone ubicated at the aneurysm centre. Moreover we notice that the highest value of β in the standard landing zones is always attained in the landing zones upstream of the aneurysmal sac. Specifically the standard landing zone which exhibits the highest risk factor is Z1 for C-I, D-I,

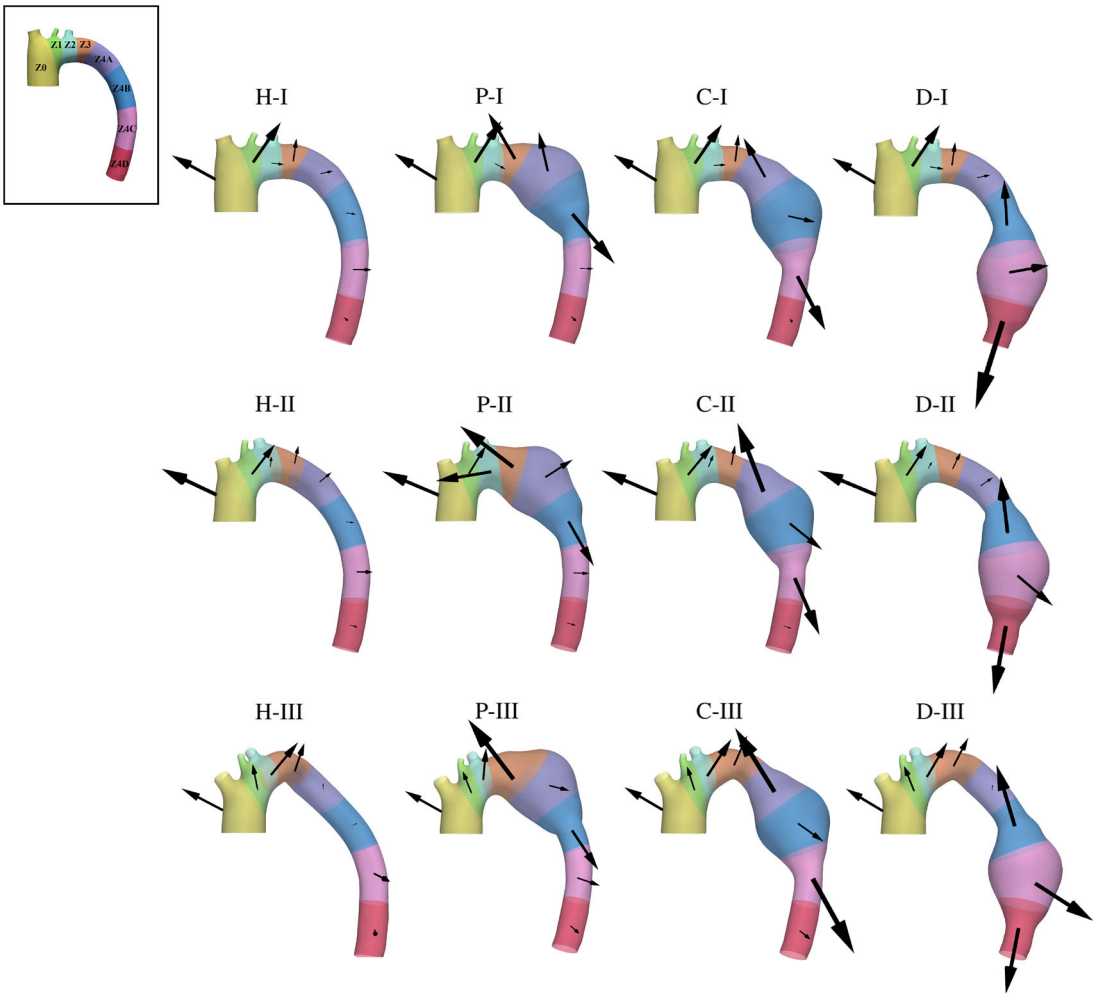

Figure 9. Ensemble drag forces $\overline{\mathbf{DF}}$ for each landing zone at the systolic peak (t = 0.165 s) in all the virtual configurations
Arrows are scaled according to $\overline{\mathbf{DF}}$ magnitude. At the top left, a representative case with landing zones is reported.

Table 5. $DF_{\parallel}$ **and** $DF_{\perp}$ **(expressed in** N^2/m^2**), and the risk factor** β **(expressed in** N^2/m^4**) computed at the systolic peak (t = 0.165 s) in each landing zone for all the virtual configurations.**

Arch type	LZ	H		P			C			D		
		$DF_{\parallel}$	$DF_{\perp}$	$DF_{\parallel}$	$DF_{\perp}$	β	$DF_{\parallel}$	$DF_{\perp}$	β	$DF_{\parallel}$	$DF_{\perp}$	β
I	Z0	1849.1	1918.8	1983.0	1824.7	4.2	1905.5	1884.5	3.7	1899.4	1831.3	3.7
	Z1	3893.8	1263.7	3918.0	1384.4	0.3	3891.8	1262.3	26.6	3800.8	1389.6	23.6
	Z2	837.5	171.9	691.6	264.2	0.7	899.1	108.6	2.4	868.5	194.8	1.6
	Z3	74.8	2776.3	3895.9	2173.6	146.7	235.8	3190.5	0.0	162.1	2897.9	0.0
	Z4A	680.7	752.3	2430.4	676.0	21.2	3597.1	447.1	84.4	636.0	805.6	0.3
	Z4B	402.3	396.3	4621.8	510.7	217.8	693.0	1145.3	0.5	3734.1	163.6	202.9
	Z4C	68.7	965.5	17.9	709.8	0.0	2920.1	578.4	124.9	348.5	1833.9	0.1
	Z4D	115.8	567.1	144.4	644.0	0.0	130.4	530.1	0.0	5188.0	12.3	3693.5
II	Z0	1669.8	3852.4	1637.9	3642.9	1.8	1568.3	3780.3	1.5	1632.8	3792.7	1.7
	Z1	2848.9	324.4	2475.2	420.3	13.9	2951.7	331.5	26.5	2776.7	408.1	19.9
	Z2	411.5	469.4	2888.5	12.6	334.7	454.5	518.3	0.2	278.4	366.0	0.1
	Z3	313.0	2015.1	6312.4	420.3	693.4	214.5	2141.8	0.0	320.6	1748.2	0.0
	Z4A	437.2	1046.1	844.8	1515.0	0.7	4870.1	877.9	186.5	438.0	960.8	0.1
	Z4B	165.3	528.6	3546.7	471.4	159.8	2072.2	826.3	24.1	4780.2	52.1	1176.6
	Z4C	53.4	1062.1	53.9	936.0	0.0	3068.6	286.1	233.8	1269.3	920.6	9.2
	Z4D	49.5	491.3	71.5	505.2	0.0	48.8	392.4	0.0	3729.6	179.6	550.5
III	Z0	928.7	2729.4	1002.4	2564.0	0.7	1068.8	2491.2	0.8	1070.6	2417.8	0.8
	Z1	1592.6	1415.6	1491.7	1469.8	2.2	1603.9	1309.7	2.9	1559.9	1570.0	2.4
	Z2	1872.9	568.2	1185.1	1085.6	1.2	2195.0	583.6	10.1	1965.4	569.5	7.4
	Z3	1394.9	903.9	2667.7	3306.1	8.8	1333.0	955.0	2.1	1476.5	18.2	20.2
	Z4A	443.2	175.3	1082.4	898.1	2.0	5757.0	125.1	810.4	383.5	182.2	0.2
	Z4B	27.9	379.6	3227.3	569.5	266.8	1362.1	656.8	18.7	4207.3	697.5	534.1
	Z4C	66.3	1455.4	60.1	1362.4	0.0	3494.8	958.3	169.3	1151.2	1797.6	4.4
	Z4D	108.4	1016.6	92.2	856.4	0.0	90.7	900.7	0.0	3644.1	8.0	1641.3

Grey cells indicate the landing zones directly affected by the pathology. Red numbers indicate the maximum value of β for each of the nine diseased configurations. Green cells identify the closest proximal and distal landing zones that we suggest for the TEVAR stent-graft anchoring.

C-II, D-II and P-III, probably due to the fact that $DF_{\parallel}$ results to be much larger than $DF_{\perp}$. Instead the highest values of β are encountered in Z2 for P-II and C-III, and in Z3 for D-III. Even though $|\overline{\mathbf{DF}}|$ in Z0 is elevated, the risk factor associated with that landing zone remains relatively low, probably because $DF_{\parallel}$ and $DF_{\perp}$ do not substantially change with respect to the healthy counterpart, and because $DF_{\perp}$ is predominant over $DF_{\parallel}$ (except for Type I configurations in which, however, $DF_{\perp}$ is comparable to $DF_{\parallel}$).

Finally, in Table 5, we highlight in green the landing zones we suggest for the stent-graft anchoring in each diseased configuration, according to the risk factor β. In all the cases, we select the proximal and distal landing zones closest to the aneurysm which exhibits low β values.

Results: patient-specific configurations

In this section, we analyse the results of the simulations obtained for the three patient-specific cases reported in 'Patient-specific geometries' section (i.e. PT-09, PT-40 and PT-71), with the attempt of confirming the outcomes found and discussed for their corresponding virtual cases (i.e. C-III, D-I and P-II, respectively) in the previous section. The aim is to verify whether predictions in terms of hemodynamic indices obtained in the ideal cases could be transferred to real aneurysmatic cases.

Hemodynamic indices

In Fig. 10, we report the ensemble velocity over seven HBs for all the patient-specific configurations at two time instants: peak systole ($t = 0.165$ s) and late diastole ($t = 0.645$ s).

At the systolic peak (Fig. 10*A*), for PT-09, we can observe a velocity field very similar to the ideal C-III case (see Fig. 6*A*): there is the presence of a high velocity jet that impinges from the region upstream of the aneurysm into the aneurysmal sac, which however disappears inside the bulging, as the latter is characterized by a considerable velocity magnitude reduction. Also for PT-40, it is possible to see great accordance with the velocity field distribution found for the virtual D-I case: a jet characterized by high velocity upstream of the aneurysm and low velocity inside

the aneurysmal sac. For PT-71, blood velocity significantly increases downstream of the aneurysm, if compared to its corresponding virtual case P-II, probably because of the vessel shrinkage at the distal aneurysm neck. Moreover the numerical simulations in the real scenarios are able to reproduce once again the vortical structure near the proximal aneurysm neck (black boxes in Fig. 10*A*), which is encountered also in the ideal configurations.

In the diastolic phase (Fig. 10*B*), in all the configurations, the streamlines show chaotic behaviour, demonstrating the presence of vortices inside the aneurysmal sac. This is in accordance with what is reported for the ideal corresponding cases (see Fig. 6*B*).

Figure 11 shows the SD of the ensemble velocity magnitude over seven HBs for all the patient-specific configurations at two different time instants: early systole (t = 0.09 s) and late diastole (t = 0.645 s). As in the virtual cases, we notice that SD is particularly high within the aneurysm, thus demonstrating great velocity fluctuations and so a likely transition to turbulence. In particular, in PT-09, SD reaches values of about 28% of the maximum ensemble velocity, in good agreement with its ideal corresponding case, in which SD reaches values of about 35% of the maximum ensemble velocity. Instead PT-40 shows lower SD values if compared with the other two patient-specific scenarios, in accordance with the study in the ideal cases that shows smaller values of SD for Type I aortic arch (see Fig. 7). PT-71 is characterized by high values of SD also downstream of the aneurysmal sac, probably caused by the narrowing of the vessel at the distal aneurysm neck.

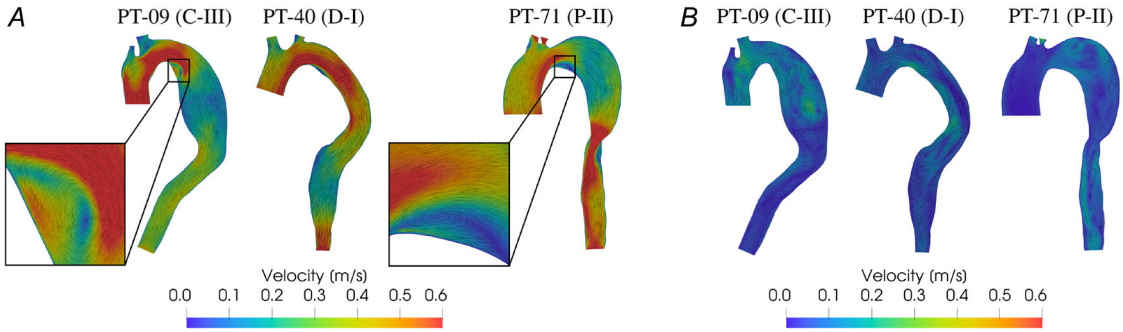

Figure 10.
(*A*) Ensemble velocity magnitude over seven HBs at the systolic peak (t = 0.165 s) in all the patient-specific configurations. Black boxes highlight the vortex forming near the proximal aneurysm neck. (*B*) Ensemble velocity magnitude over seven HBs at late diastole (t = 0.645 s) in all the patient-specific configurations. In the brackets, we report the corresponding virtual scenario.

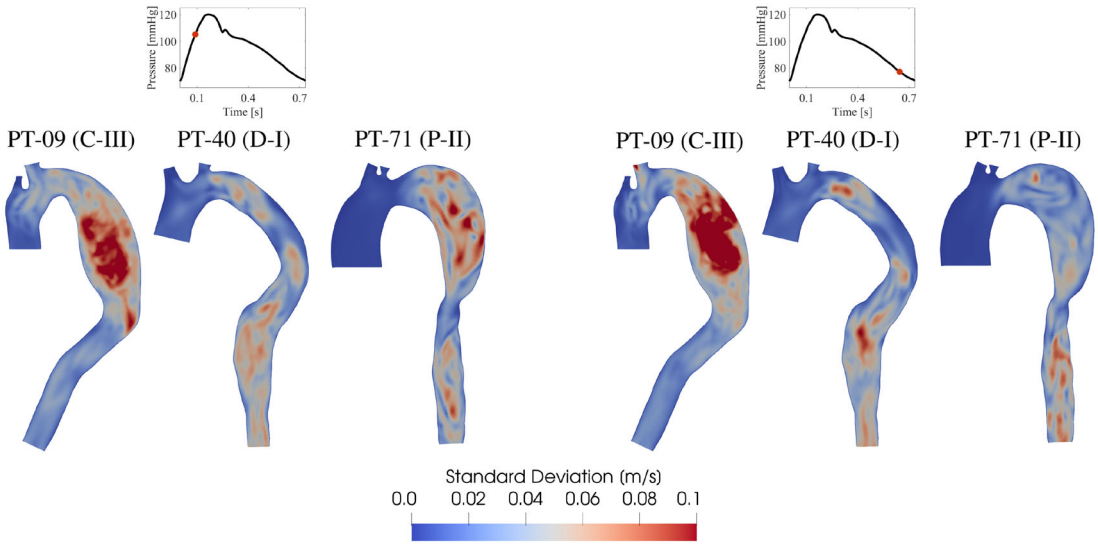

Figure 11. Standard deviation (SD) of the ensemble velocity magnitude over seven HBs in all the real configurations at two time instants
(Left) early systole (t = 0.09 s) and (right) late diastole (t = 0.645 s). In the brackets, we report the corresponding virtual scenario.

Drag force magnitude and orientation

Figure 12 shows the ensemble drag forces $\overline{\mathbf{DF}}$ magnitude and orientation in each landing zone for all the patient-specific configurations. As it happens for the corresponding virtual cases (i.e. C-III, D-I and P-II, see Fig. 9 and Table 5), the landing zones ubicated in correspondence of the proximal and distal aneurysm necks show the greatest $|\overline{\mathbf{DF}}|$. Moreover we observe that the proximal standard landing zone which exhibits the highest $|\overline{\mathbf{DF}}|$ is Z0 for PT-71 (consistently with P-II), while it is Z1 for PT-09 and PT-40 (consistently with D-I). In addition, in accordance with the ideal cases, we observe that in Z1, $|\overline{\mathbf{DF}}|$ is maximum for PT-40 and minimum for PT-71, whereas in Z2, the maximum is attained for PT-09. In addition, in the landing zones ubicated in correspondence of the aneurysm necks, $\overline{\mathbf{DF}}$ is mainly oriented towards the vessel centreline direction, consistently with the corresponding virtual scenarios. In all the patient-specific configurations, $\overline{\mathbf{DF}}$ in Z0 is mainly oriented towards the heart, coherently with the virtual cases.

Regarding PT-09, $\overline{\mathbf{DF}}$ in Z4A and $\overline{\mathbf{DF}}$ in Z4C point upwards and downwards, respectively, in good agreement with C-III. Also the orientation of $\overline{\mathbf{DF}}$ in Z4B, which is localized in the aneurysm centre, is similar with the ideal corresponding configuration. Regarding the proximal standard landing zones, $\overline{\mathbf{DF}}$ in Z1, Z2 and Z3 is mainly directed in the cranial direction, in good agreement with C-III.

In PT-40, we notice that the orientation of $\overline{\mathbf{DF}}$ in Z4D is almost the same as in D-I, whereas this does not hold for the direction in Z4B and in Z4C, probably because of the more pronounced curvature that characterizes the real DTA. However $\overline{\mathbf{DF}}$ direction in the proximal standard landing zones is consistent with D-I.

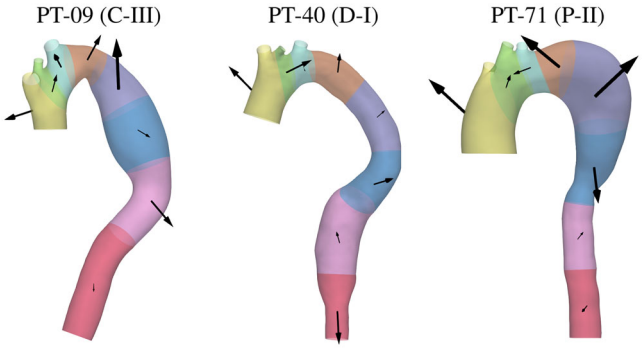

Figure 12. Ensemble drag forces $\overline{\mathrm{DF}}$ of each landing zone at the systolic peak (t = 0.165 s) in all the patient-specific configurations
Arrows are scaled according to $\overline{\mathbf{DF}}$ magnitude. In the brackets, we report the corresponding virtual scenario.

For PT-71 we observe the same $\overline{\mathbf{DF}}$ orientation of P-II in all the three landing zones directly affected by the pathology (i.e. Z3, Z4A and Z4B). In Z2, $\overline{\mathbf{DF}}$ results to be mainly directed towards the heart, while in Z1, it is mainly oriented along the cranial direction, as it happens in its corresponding ideal case.

In Table 6 we report the values of $DF_{\parallel}$ and $DF_{\perp}$ in each landing zone for all the patient-specific configurations. As in the virtual scenarios (see Table 5), in the landing zones located in correspondence of the aneurysm necks, $DF_{\parallel}$ is greater than $DF_{\perp}$ in all the three cases, except for Z4C in PT-09, probably because of the slight curvature of its DTA. In the landing zone ubicated at the aneurysm centre, $DF_{\parallel}$ results to be larger than $DF_{\perp}$ in PT-40 and PT-09 (as in C-III), in contrast to PT-71, which is however consistent with what is observed for P-II. Regarding the standard landing zones located at the aortic arch, in Z0, $DF_{\perp}$ results to be higher than $DF_{\parallel}$ in PT-09 (as in C-III) and PT-40, but not in PT-71. In Z1, $DF_{\parallel}$ is predominant over $DF_{\perp}$ in all the three cases (as in the virtual scenarios), and in Z2, $DF_{\parallel}$ exceeds $DF_{\perp}$ in PT-71 (as in P-II), while the opposite happens in PT-09 and PT-40.

In Table 6, we report also the risk factor β in each landing zone for all the three real configurations. Consistently with the ideal cases, the highest risk factor values (red numbers in Table 6) are always found in correspondence of the aneurysmal sac (grey cells in Table 6). Moreover the standard landing zone with the highest value of β results to be Z1 for PT-09 and PT-40 and Z2 for PT-71, consistently with their virtual counterparts (except for PT-09).

In Table 6, as a very preliminary result, we highlight in green the landing zones we suggest for the stent-graft anchoring in all the three patient-specific configurations. As done for the virtual cases, we choose as possible landing zones those closest to the aneurysmal sac and with a low value of β. Notice the excellent agreement with the study of the ideal cases.

Discussion

On the novelties of the study

This study presents a detailed description of the hemodynamics and wall state of stress of DTAAs in virtual and patient-specific scenarios, also providing valuable insights on the forces exerted by the blood flow on the aortic wall. To do this we performed a 3D FSI analysis with a turbulence model, to capture transition to turbulence highly characterizing thoracic aortic blood flow, and distinguishing the elastic properties of the healthy and aneurysmatic portion of the vessel.

To the best of our knowledge, this is the first attempt where such a sophisticated model has been used to

Table 6. $DF_{\parallel}$ and $DF_{\perp}$ (expressed in N/m^2), and the risk factor β (expressed in N^2/m^4) computed at the systolic peak (t = 0.165 s) in each landing zone for all the patient-specific configurations.

LZ	PT-09 (C-III)			PT-40 (D-I)			PT-71 (P-II)		
	$DF_{\parallel}$	$DF_{\perp}$	β	$DF_{\parallel}$	$DF_{\perp}$	β	$DF_{\parallel}$	$DF_{\perp}$	β
Z0	705.2	2221.9	0.2	608.0	2037.6	0.1	2002.6	1387.0	5.3
Z1	1841.9	1099.5	4.7	2960.0	100.2	41.5	1011.6	631.7	0.8
Z2	683.7	2141.6	0.2	140.4	399.3	0.0	2213.9	108.6	51.3
Z3	742.6	2078.4	0.2	622.1	1188.5	0.8	3596.3	1330.4	72.1
Z4A	3615.6	739.6	82.6	23.3	739.5	0.0	823.7	2217.6	0.6
Z4B	827.4	206.8	7.5	1588.6	526.2	8.7	2286.4	280.5	55.5
Z4C	481.9	2065.9	0.3	586.7	243.8	1.6	336.3	231.6	0.3
Z4D	289.7	50.3	0.3	2162.5	13.2	258.6	243.2	160.6	0.2

Grey cells indicate the landing zones directly affected by the pathology. Red numbers indicate the maximum value of β for each of the three diseased configurations. Green cells identify the closest proximal and distal landing zones that we suggest for the TEVAR stent-graft anchoring. In the brackets, we report the corresponding virtual scenario.

obtain relevant outcomes in terms of force distribution in DTAAs. Moreover this is the first time where an hemodynamic analysis has been performed for several DTAA configurations with different aneurysm locations and aortic arch types.

On the physiological and pathophysiological relevance of the study

The presence of the aneurysm causes an increase in peak pressure both within the aneurysmal sac and in the downstream portion of DTA, while it provokes a sudden change in pressure values at the proximal and distal necks of the bulging (see Fig. 5*A*). These results are in good agreement with the computational studies conducted by Etli et al. (2021) and by Dadras et al. (2023). The former reported a pressure increase from a normal subject to two TAA cases during the systolic peak, while the latter showed a homogeneously higher pressure within the aneurysm, with a sudden change in pressure values at the distal neck of the sac. We argue that the peak pressure increase could be due to the higher stiffness imposed to the aneurysmal wall, consistently with what was found by Campobasso et al. (2018). Considering the increase in peak pressure inside the aneurysmal sac, we can presume that the presence of DTAA may enhance the load on the aortic wall, and thus, potentially increase the risk of aneurysm enlargement and rupture (Choke et al., 2005).

Thanks to our model, which allows us to account for different Young's moduli for the healthy and aneurysmatic portion of the vessel, we obtain that the middle cross-sectional area variation within one HB is halved when passing from the healthy to the diseased TA (see Fig. 4*B*). In addition, given the higher stiffness of the aneurysmal sac, the aneurysmatic wall is subjected to greater internal stresses, in accordance with the VMSs distribution (see Fig. 8*B*), increasing the likelihood of rupture. In particular our numerical results show that the most stressed regions are the proximal and distal aneurysm necks, in which, therefore, we speculate that the rupture is more likely to occur, whereas the area at the centre of the aneurysmal sac shows lower VMS values. These results are in accordance with what was reported by Silva et al. (2023), who found that peak VMS did not occur in the larger diameter aneurysm section, but at the aneurysm necks.

At the systolic peak, within the aneurysmal sac, blood flow is characterized by disordered streamlines, demonstrating the presence of tiny vortices on the lesser curvature side near the proximal aneurysm neck (see Fig. 6*A*), which might be regions of blood re-circulation. These re-circulation regions favour the formation of blood stagnation (Ong et al., 2019) and increase in size with the degree of aortic arch curvature (i.e. from arch Types I–III), resulting more evident in P-III and C-III. Besides, C-III scenario presents another vortical structure within the aneurysmal sac, further enhancing the blood re-circulation. The latter is strictly related to aneurysm rupture (Numata et al., 2016) and intraluminal thrombus (ILT) formation (Ong et al., 2018), confirming that sharp curvature (i.e. Type III), at the inner side wall of the aortic arch, causes flow separation and the rolling up of the shear layer to form conditions facilitating ILT formation and thus aneurysm rupture (Numata et al., 2016; Ong et al., 2018). In the same regard Arzani et al. (2014) found that very low OSI values (<0.1) may identify regions where ILT formation is more likely to occur. Interestingly the aneurysmal sac in C-III is characterized entirely by very low OSI values. More generally, in P and C configurations, low OSI values are attained in the regions where the re-circulations are observed. On the other hand, D configurations, which instead exhibit greater values of OSI in the region near the proximal aneurysm neck, show

indeed re-circulation regions with a much smaller size in such an area.

On the contrary the OSI distribution exhibits high values in several regions within the aneurysmal sac and at the aneurysm's necks in all the configurations (see Fig. 8*A*), in good agreement with Numata et al. (2016). This means that all the configurations under study may be at risk in terms of atherosclerotic plaque formation (Zeng & Li, 2013). This is a serious risk as plaque can burst or rupture the inner wall intima continuing up to the adventitia (Febina et al., 2018). Specifically we notice that for proximal aneurysms (P configurations), it seems that the region most at risk is the aneurysmal sac, whereas for distal aneurysms (D configurations), the region most at risk reveals to be the proximal aneurysm neck or even the healthy portion of DTA upstream the aneurysm (D-III).

The distribution of the SD of the ensemble velocity magnitude allows us to quantify and localize the velocity fluctuations among the HBs and thus regions of transition to turbulence (Vergara et al., 2017). SD reaches its highest values within the aneurysm (see Fig. 7), confirming that transition to turbulence develops inside the sac, especially during blood deceleration phase. This disordered behaviour of the velocity field may be caused by the sudden expansion of the flow stream, due to abrupt vessel enlargement in correspondence of the aneurysmal sac (Tan et al., 2009). Turbulent flow could generate higher stresses on the aneurysm wall, if compared with laminar flow, causing an increasing rate of wall dilation, thus enhancing turbulence itself, establishing a mechanism for aneurysm dilation (Khanafer et al., 2007). We also notice that, as the aortic arch curvature increases, the flow regime becomes more unstable and tends more towards a regime of transition to turbulence. Indeed, even in the healthy case H-III, it is possible to identify a region with high turbulence in the descending portion of the vessel. Probably, in Type III configurations, the steep aortic arch curvature provokes an high-velocity jet in the areas upstream of the aneurysmal sac, which promotes transition to turbulence (Tan et al., 2009).

Towards preliminary indications for TEVAR procedure

Drag forces were intensively analysed to assess the stress state of the aorta after TEVAR implantation (Fung et al., 2008; Figueroa & Zarins, 2011; Krsmanovic et al., 2014). Here we want to investigate such quantities to evaluate the state of stress of the aneurysmatic cases before the insertion of the stent-graft, with the hope that this analysis could support TEVAR planning and the prediction of outcomes, provided that future studies will be addressed to establish such relationship. Specifically, in this study, we have evaluated the magnitude and orientation of drag forces in each landing zone intended by the MALAN classification (Marrocco-Trischitta et al., 2017).

The comparison between aneurysmal and healthy TA showed no differences in terms of drag forces magnitude and orientation in the landing zones not directly involved by the pathology (i.e. standard landing zones). Instead the presence of the aneurysmal sac causes an increase in drag force magnitude and a gradual shift in their orientation towards the vessel centreline in the landing zones ubicated at the proximal and distal aneurysm necks. In particular, in such zones, drag force magnitude results to be from three up to six times higher than those in the adjacent zones, consistently with the pressure distribution and with what was reported by Marrocco-Trischitta et al. (2019). Moreover, considering the standard landing zones, the drag forces with the greatest magnitude are localized in the proximal landing zones involving the aortic arch (i.e. Z1, Z2 and Z3), in good accordance with what was found by Marrocco-Trischitta et al. (2018). The landing zones ubicated at the aortic arch exhibit larger values of the resultant drag forces because of the restricted surface area and the higher pressure values that characterize the former zones. The resultant drag force orientation largely depends on the aortic anatomic features (Figueroa et al., 2009; Kandail et al., 2014; Marrocco-Trischitta et al., 2018). Indeed changes in the shape of a certain landing zone cause changes in the direction of the surface normals, consequently leading to a shift in the resultant drag force orientation. For instance, if the landing zone presents some curvatures (such as the aneurysm neck), there is a deflection of the resultant drag forces orientation.

In what follows, we go deeper in our preoperative analysis to understand whether and how it could provide some preliminary results in relation to the identification of the best landing zones for the stent-graft sealing. This could be in future very useful for clinicians to have information on how to perform the anchorage before TEVAR procedure. According to Domanin et al. (2021), during the planning phase for TEVAR procedure, it may be useful to estimate in advance the hemodynamic drag forces, due to the blood flow, acting on the aortic wall. Indeed, a notably challenging hemodynamics, typical of certain regions of the aneurysmatic DTA, may cause the generation of particularly hostile drag forces, which potentially lead to an insufficient proximal or distal sealing likely causing the stent-graft migration (Figueroa et al., 2009).

To take into account all the threatening conditions that may lead to endograft migration (see 'Towards a preliminary TEVAR analysis' section), we propose a risk factor β: a single index able to summarize all the dangerous conditions to classify each landing zone based on its risk of migration. The greatest value of β is always attained in the landing zones located in correspondence of the proximal and distal aneurysm necks. This behaviour

could be explained by two mechanisms as follows: first, because in such regions the drag force component parallel to the vessel centreline is always greater than the normal one; second, because of the noticeable variation in the drag forces with respect to the healthy condition. For these reasons, this landing zones should be avoided for the stent-graft sealing. Moreover the highest value of β in the standard landing zones is always attained in the landing zones upstream of the aneurysmal sac. Indeed, in these regions, it is often the case that the parallel component results to be larger than the perpendicular one, even though there is no substantial change between the diseased and the corresponding healthy cases. In particular, for Type III configurations, the parallel component is always predominant over the perpendicular one in all the three landing zones ubicated at the aortic arch, even though its values are not always the highest if compared with Type I and II cases. According to β, the risk of endograft migration in Z1 decreases when passing from Type I to Type III aortic arch, whereas it is maximum in Z2 and Z3 for Type III configurations, except for P scenarios where the maximum and minimum risk is reached in P-II and P-I, respectively. Our results are also in agreement with the less frequency of TEVAR complications observed for proximal sealing performed in Z0 (Melissano et al., 2007). However it is important to recall that an anchorage at that level would require the bypass of all three supraortic vessels, making the surgery more challenging (Milewski et al., 2010).

Considering the aforementioned observations, regarding the proximal stent-graft sealing (see green cells in Table 5), we notice the following:

- For D configurations, regardless of the arch type, it would be better to choose Z4A as proximal landing zone, as it is not located at the aortic arch and it has always a perpendicular component larger than the parallel one. However, we notice that, especially for D-III, Z4A features large values of OSI, that is, high risk of plaque formation; for this reason, the effective choice of this landing zone for the stent-graft anchoring should account this risk.
- For P-I, P-III and C-II configurations, Z2 seems to be the most suitable proximal landing zone, as it shows a slight difference between the parallel and the perpendicular components, both with reduced magnitude, if compared with the neighbouring landing zones.
- For P-II configuration, Z0 could be the best choice for the proximal sealing, as it has the lowest β value, while Z1 and Z2 are characterized by a too high parallel component in relation to the perpendicular one.
- For C-I and C-III configurations, the better choice could be Z3 because, in the former case, it has a negligible value of β, while, in the latter case, it exhibits the lowest parallel and perpendicular component combination with respect to the nearby landing zones.

This study on DTAAs may have significant implications in the clinical field. First, it emphasizes the need to evaluate hemodynamics and structural stresses when aiming to optimize the biomedical device used in TEVAR or in other procedures. Second, the analysis of VMSs and drag forces offers insights into potential failure points of the stent-graft, which need to be considered during the surgical decision-making process, as blood forces and stress distributions are crucial for the endograft deployment and consequently for the patient's post-operative outcomes. Moreover our FSI computational model can be applied to various vascular fields (both medical and surgical) allowing for predictive analyses that anticipate problems before physical prototypes are built and/or validated, and before vascular endograft is implanted. Furthermore the consideration of complex anatomical variations (i.e. different aortic arch types or aneurysm ubications) illustrates the importance of adaptable designs, relevant to medical device companies. Our computational framework can be applied also to patient-specific cases, having the potential for customized solutions, and ultimately helping to improve the stent-graft performances. Our FSI model can serve as the foundation for a routine procedure aimed at optimizing TEVAR procedure planning with consideration for patient-specific geometrical factors. More generally, understanding hemodynamic implications on biomedical devices can guide their regulatory standards, ensuring that they meet safety criteria, and the integration of these insights into the medical field can enhance the reliability and effectiveness of solutions across multiple vascular and engineering applications.

On the validity of the analysis on patient-specific cases

In this study we have applied our computational model also to three patient-specific configurations, showing that the model and the numerical results obtained are also valid for real cases. In particular it is possible to observe that the main features found for the ideal cases, that is, the high-velocity jet in the upstream region of the aneurysmal sac, the re-circulation area near the proximal aneurysm neck at the systolic peak, as well as the relatively high velocity vortex at the late diastole, hold true for patient-specific scenarios. Moreover all the three patient-specific configurations are characterized by high SD values at different time instants of the HB, in good accordance with their corresponding virtual cases. Finally the analysis in the real cases highlights an excellent agreement regarding the distribution of forces along TA, with respect to the ideal cases analysis. Indeed the main

results on drag forces, underlined for the virtual cases, are still valid for the real patient-specific configurations.

Specifically, we found that, also for the real cases, Type III aortic arch (PT-09) is the most prone to transition to turbulence, confirming what is observed in the ideal cases, particularly in C-III (see Fig. 11). Moreover the results of the index β (see Table 6) confirm that, for all the three cases, maximum values are attained for the aneurysmatic landing zones (grey cells in Table 6) and the suggested landing zones for the stent-graft anchoring, characterized by low values of β (green cells in Table 6), are in accordance with the results of the ideal cases (see Table 5).

These findings have a great clinical relevance. Indeed, once the nine diseased cases have been simulated and analysed, it is possible to make a general *a priori* assessment of the hemodynamics and internal wall stresses of any real patient-specific case on the basis of the virtual cases analysis.

Despite the great similarities between the results of the real and ideal configurations, it is important also to draw attention to the differences found. In particular the main differences are found in the orientation of drag forces and, consequently, in the β values, probably because of the higher tortuosity of the landing zones in the real configurations, which tends to affect more the orientation of drag forces. However, these differences are not surprising, as each patient's TA has its peculiar and unique geometrical features, which differ from case to case, and thus it is not feasible to build an ideal model that perfectly fits every patient's configuration. Anyway the purpose of an ideal model is to replicate the main characteristics of reality by simplifying its geometric complexity so as to provide reliable results. From this perspective our results show that the analysis performed over the ideal cases seems to be suitable to capture the main hemodynamic features of any patient-specific cases.

Major outcomes, limitations and future developments

In what follows, we try to underline the major outcomes emerged by our analysis:

- The aneurysmal sac is characterized by higher peak pressure values and VMSs with respect to the healthy condition, provoking large loads in the internal wall thus inducing a risk of aneurysm rupture. Moreover the aneurysm shows very low values of blood velocity and several blood re-circulation regions, associated with low values of OSI, increasing the risk of ILT formation. On the contrary other regions of the aneurysm are associated with large OSI values, increasing the risk of atherosclerotic plaque formation. This may be relevant in the proximal aneurysm neck and in the healthy portion of DTA upstream of the aneurysmal sac for D configurations.
- Configurations with a steeper aortic arch (i.e. Type III) present a more chaotic hemodynamics, with disordered streamlines and higher likelihood of transition to turbulence. The latter may be an index of increased rupture risk for Type III. However pressure results suggest that Types I and II could be the most critical.
- The presence of the aneurysmal sac causes the increase in ensemble drag force magnitude, with respect to the healthy condition, and the shift in their orientation towards the vessel centreline. The greatest increase in drag forces magnitude, with respect to the healthy condition, is attained in configurations with a distal aneurysm. Regarding the regions not directly affected by the pathology, the highest drag force magnitude is encountered in the landing zones upstream of the aneurysmal sac. In such regions it is common for the drag force parallel component to exceed the normal one.
- The risk of endograft migration at the level of the proximal sealing decreases as the aortic arch curvature increases (i.e. from Type I to Type III) in Z1, while it is maximum in Z2 and Z3 for Type III configurations.
- The numerical results found for the real patient-specific cases are in good agreement with the results of the virtual cases.

This study presents some limitations which are summarized below:

- The pressure-wave employed as an inlet boundary condition for the real cases is taken from literature. A future development to assess the validity of the ideal analysis for real cases could be the inclusion for the latter of a patient-specific inlet condition derived from clinical measurements (e.g. blood flow rate or pressure over time).
- The model used for the mathematical representation of the material of the aortic wall is the linear elasticity. However more sophisticated and realistic material models could be used, such as hyperelasticity or a fibre-based model. In addition, in this work, blood is considered as a Newtonian fluid, even though it is known that blood is a non-Newtonian, shear-thinning liquid (Gasser et al., 2024). For this reason, in the future, to better represent the hemodynamics at low shear rate (typical of the aneurysmal sac), one can opt for non-Newtonian models (Berguer et al., 2006).
- The virtual cases are willingly designed with fusiform aneurysms and with low DTA tortuosity, to evaluate the influence of the type of arch and ubication of the aneurysm only. In the future we plan to analyse other anatomical complexities, such as DTA tortuosity or saccular aneurysms.

- We apply our computational analysis to three patients who underwent TEVAR. Because this is a computational study, and not a statistical one, we design an *a priori* model, supported by imaging data and based on the physical principles of fluid dynamics, and not an a posteriori model based only on clinical measurements. Indeed our intention is not to conduct extensive statistical analyses, but instead our focus is on presenting a proof-of-concept to highlight the potential of our proposed methodology, which proves to be well suited for systematic replication on a patient-specific basis. In this respect the application to a relative low number of patients seems to be suitable for our purposes. Investigations involving a larger number of patients will be considered in future studies to achieve more comprehensive insights about our analysis.
- The lack of follow-up data does not make it possible to validate our prediction regarding the possible TEVAR procedure outcomes of the patient-specific cases. Thus, for the future, it will be needed to analyse cases whose evolution, in terms of possible TEVAR migration, is known.
- The risk factor β is designed to consider only the threatening conditions that could lead to stent-graft migration. In the future it will be interesting to assess the risk of endoleak formation by designing a new appropriate index or by adapting β.
- The assessment of the risk of stent-graft migration is made only on the basis of the hemodynamic drag forces. As future development, it could be of interest to consider also structural parameters (e.g. VMS).

In conclusion we believe that the analysis presented in this paper could add a new piece to the mosaic of the research to better understand the pathophysiology of DTAAs, and to provide preliminary information on TEVAR possible outcomes.

References

Africa, P. C. (2022). lifex: A flexible, high performance library for the numerical solution of complex finite element problems. *SoftwareX*, **20**, 101252.

Africa, P. C., Fumagalli, I., Bucelli, M., Zingaro, A., Fedele, M., Dede', L., & Quarteroni, A. (2024). lifex-cfd: An open-source computational fluid dynamics solver for cardiovascular applications. *Computer Physics Communications*, **296**, 109039.

Ahrens, J., Geveci, B., Law, C., Hansen, C., & Johnson, C. (2005). 36-paraview: An end-user tool for large-data visualization. In *The visualization handbook*, (pp. 717–731). Elsevier.

Alastruey, J., Parker, K. H., Sherwin, S. J. (2012). Arterial pulse wave haemodynamics. In *11th international conference on pressure surges* (Vol. **30**, pp. 401–443). Virtual PiE Led t/a BHR Group.

Alastruey, J., Passerini, T., Formaggia, L., & Peiró, J. (2012). Physical determining factors of the arterial pulse waveform: Theoretical analysis and calculation using the 1-D formulation. *Journal of Engineering Mathematics*, **77**, 19–37.

Alastruey, J., Xiao, N., Fok, H., Schaeffter, T., & Figueroa, C. A. (2016). On the impact of modelling assumptions in multi-scale, subject-specific models of aortic haemodynamics. *Journal of The Royal Society Interface*, **13**(119), 20160073.

Arzani, A., Suh, G.-Y., Dalman, R. L., & Shadden, S. C. (2014). A longitudinal comparison of hemodynamics and intraluminal thrombus deposition in abdominal aortic aneurysms. *American Journal of Physiology-Heart and Circulatory Physiology*, **307**(12), H1786–H1795.

Azadani, A. N., Chitsaz, S., Mannion, A., Mookhoek, A., Wisneski, A., Guccione, J. M., Hope, M. D., Ge, L., & Tseng, E. E. (2013). Biomechanical properties of human ascending thoracic aortic aneurysms. *The Annals of thoracic surgery*, **96**(1), 50–58.

Belvroy, V. M., Romarowski, R. M., van Bakel, T. M., van Herwaarden, J. A., Bismuth, J., Auricchio, F., Moll, F. L., & Trimarchi, S. (2020). Impact of aortic tortuosity on displacement forces in descending thoracic aortic aneurysms. *European Journal of Vascular and Endovascular Surgery*, **59**(4), 557–564.

Berguer, R., Bull, J. L., & Khanafer, K. (2006). Refinements in mathematical models to predict aneurysm growth and rupture. *Annals of the New York Academy of Sciences*, **1085**(1), 110–116.

Biasetti, J., Gasser, T. C., Auer, M., Hedin, U., & Labruto, F. (2010). Hemodynamics of the normal aorta compared to fusiform and saccular abdominal aortic aneurysms with emphasis on a potential thrombus formation mechanism. *Annals of Biomedical Engineering*, **38**, 380–390.

Borghi, A., Wood, N. B., Mohiaddin, R. H., & Xu, X. Y. (2008). Fluid-solid interaction simulation of flow and stress pattern in thoracoabdominal aneurysms: A patient-specific study. *Journal of Fluids and Structures*, **24**(2), 270–280.

Bossone, E., & Eagle, K. A. (2021). Epidemiology and management of aortic disease: Aortic aneurysms and acute aortic syndromes. *Nature Reviews Cardiology*, **18**(5), 331–348.

Boussel, L., Rayz, V., McCulloch, C., Martin, A., Acevedo-Bolton, G., Lawton, M., Higashida, R., Smith, W. S., Young, W. L., & Saloner, D. (2008). Aneurysm growth occurs at region of low wall shear stress: Patient-specific correlation of hemodynamics and growth in a longitudinal study. *Stroke*, **39**(11), 2997–3002.

Boyd, A. J., Kuhn, D. C., Lozowy, R. J., & Kulbisky, G. P. (2016). Low wall shear stress predominates at sites of abdominal aortic aneurysm rupture. *Journal of Vascular Surgery*, **63**(6), 1613–1619.

Bucelli, M., Dede, L., Quarteroni, A., Vergara, C. (2023). Partitioned and monolithic algorithms for the numerical solution of cardiac fluid-structure interaction. *Communications in Computational Physics*, **32**(5), 1217–1256.

Callaghan, F., Karkouri, J., Broadhouse, K., Evin, M., Fletcher, D., & Grieve, S. (2015). Thoracic aortic aneurysm: 4D flow MRI and computational fluid dynamics model. *Computer Methods in Biomechanics and Biomedical Engineering*, **18**(S1), 1894–1895.

Campobasso, R., Condemi, F., Viallon, M., Croisille, P., Campisi, S., & Avril, S. (2018). Evaluation of peak wall stress in an ascending thoracic aortic aneurysm using FSI simulations: Effects of aortic stiffness and peripheral resistance. *Cardiovascular Engineering and Technology*, **9**, 707–722.

Carpenter, H. J., Ghayesh, M. H., Zander, A. C., & Psaltis, P. J. (2023). On the nonlinear relationship between wall shear stress topology and multi-directionality in coronary atherosclerosis. *Computer Methods and Programs in Biomedicine*, **231**, 107418.

Carpenter, H. J., Gholipour, A., Ghayesh, M. H., Zander, A. C., & Psaltis, P. J. (2020). A review on the biomechanics of coronary arteries. *International Journal of Engineering Science*, **147**, 103201.

Choke, E., Cockerill, G., Wilson, W., Sayed, S., Dawson, J., Loftus, I., & Thompson, M. (2005). A review of biological factors implicated in abdominal aortic aneurysm rupture. *European Journal of Vascular and Endovascular Surgery*, **30**(3), 227–244.

Clift, P. F., & Cervi, E. (2020). A review of thoracic aortic aneurysm disease. *Echo Research & Practice*, **7**(1), R1–R10.

Coats, A. (1990). Doppler ultrasonic measurement of cardiac output: Reproducibility and validation. *European Heart Journal*, **11**(SI), 49–61.

Critchley, L. A., & Critchley, J. A. (1999). A meta-analysis of studies using bias and precision statistics to compare cardiac output measurement techniques. *Journal of Clinical Monitoring and Computing*, **15**, 85–91.

Crosetto, P., Reymond, P., Deparis, S., Kontaxakis, D., Stergiopulos, N., & Quarteroni, A. (2011). Fluid–structure interaction simulation of aortic blood flow. *Computers & Fluids*, **43**(1), 46–57.

Dadras, R., Jabbari, A., Asl, N. K., Soltani, M., Rafiee, F., Parsaee, M., Golchin, S., Pouraliakbar, H., Sadeghipour, P., & Alimohammadi, M. (2023). In-silico investigations of haemodynamic parameters for a blunt thoracic aortic injury case. *Scientific Reports*, **13**(1), 8355.

Di Martino, E. S., Guadagni, G., Fumero, A., Ballerini, G., Spirito, R., Biglioli, P., & Redaelli, A. (2001). Fluid-structure interaction within realistic three-dimensional models of the aneurysmatic aorta as a guidance to assess the risk of rupture of the aneurysm. *Medical Engineering & Physics*, **23**(9), 647–655.

Domanin, M., Bissacco, D., Romarowsky, R. M., Conti, M., Auricchio, F., Ferraresi, M., & Trimarchi, S. (2021). Drag forces after thoracic endovascular aortic repair. General review of the literature. *Annals of Vascular Surgery*, **75**, 479–488.

Donea, J., Huerta, A., Ponthot, J.-P., & Rodríguez-Ferran, A. (2004). Arbitrary Lagrangian-Eulerian methods. In *Encyclopedia of computational mechanics*. Wiley.

Doyle, B. J., Callanan, A., Burke, P. E., Grace, P. A., Walsh, M. T., Vorp, D. A., & McGloughlin, T. M. (2009). Vessel asymmetry as an additional diagnostic tool in the assessment of abdominal aortic aneurysms. *Journal of Vascular Surgery*, **49**(2), 443–454.

Duronio, F., & Di Mascio, A. (2023). Blood flow simulation of aneurysmatic and sane thoracic aorta using openFOAM CFD software. *Fluids*, **8**(10), 272.

Elefteriades, J. A., & Botta, D. M. (2009). Indications for the treatment of thoracic aortic aneurysms. *Surgical Clinics*, **89**(4), 845–867.

Elefteriades, J. A., & Farkas, E. A. (2010). Thoracic aortic aneurysm: Clinically pertinent controversies and uncertainties. *Journal of the American College of Cardiology*, **55**(9), 841–857.

Etli, M., Canbolat, G., Karahan, O., & Koru, M. (2021). Numerical investigation of patient-specific thoracic aortic aneurysms and comparison with normal subject via computational fluid dynamics (CFD). *Medical & Biological Engineering & Computing*, **59**, 71–84.

Febina, J., Sikkandar, M. Y., & Sudharsan, N. M. (2018). Wall shear stress estimation of thoracic aortic aneurysm using computational fluid dynamics. *Computational and Mathematical Methods in Medicine*, **2018**(1), 7126532.

Figueroa, C. A., Taylor, C. A., Chiou, A. J., Yeh, V., & Zarins, C. K. (2009). Magnitude and direction of pulsatile displacement forces acting on thoracic aortic endografts. *Journal of Endovascular Therapy*, **16**(3), 350–358.

Figueroa, C. A., & Zarins, C. K. (2011). Computational analysis of displacement forces acting on endografts used to treat aortic aneurysms. In *Biomechanics and mechano-biology of aneurysms* (pp. 221–246). Springer.

Fillinger, M. F., Marra, S. P., Raghavan, M. L., & Kennedy, F. E. (2003). Prediction of rupture risk in abdominal aortic aneurysm during observation: Wall stress versus diameter. *Journal of Vascular Surgery*, **37**(4), 724–732.

Frauenfelder, T., Lotfey, M., Boehm, T., & Wildermuth, S. (2006). Computational fluid dynamics: Hemodynamic changes in abdominal aortic aneurysm after stent-graft implantation. *Cardiovascular and Interventional Radiology*, **29**, 613–623.

Fung, G. S., Lam, S., Cheng, S. W., & Chow, K. (2008). On stent-graft models in thoracic aortic endovascular repair: A computational investigation of the hemodynamic factors. *Computers in Biology and Medicine*, **38**(4), 484–489.

Gao, F., Guo, Z., Sakamoto, M., & Matsuzawa, T. (2006). Fluid-structure interaction within a layered aortic arch model. *Journal of Biological Physics*, **32**, 435–454.

Gasser, T. C., Avril, S., & Elefteriades, J. A. (2024). *Biomechanics of the aorta*. Elsevier.

Goldfinger, J. Z., Halperin, J. L., Marin, M. L., Stewart, A. S., Eagle, K. A., & Fuster, V. (2014). Thoracic aortic aneurysm and dissection. *Journal of the American College of Cardiology*, **64**(16), 1725–1739.

Inc., A. (2019). *Autodesk meshmixer*. http://www.meshmixer.com

Ishimaru, S. (2004). Endografting of the aortic arch. *Journal of Endovascular Therapy*, **11**(S6), II-62–II-71.

Izzo, R., Steinman, D., Manini, S., & Antiga, L. (2018). The vascular modeling toolkit: A Python library for the analysis of tubular structures in medical images. *Journal of Open Source Software*, **3**(25), 745.

Johnson, A. A., & Tezduyar, T. E. (1994). Mesh update strategies in parallel finite element computations of flow problems with moving boundaries and interfaces. *Computer Methods in Applied Mechanics and Engineering*, **119**(1-2), 73–94.

Kandail, H., Hamady, M., & Xu, X. Y. (2014). Patient-specific analysis of displacement forces acting on fenestrated stent grafts for endovascular aneurysm repair. *Journal of Biomechanics*, **47**(14), 3546–3554.

Khanafer, K. M., Bull, J. L., Upchurch Jr, G. R., & Berguer, R. (2007). Turbulence significantly increases pressure and fluid shear stress in an aortic aneurysm model under resting and exercise flow conditions. *Annals of Vascular Surgery*, **21**(1), 67–74.

Krsmanovic, D., Koncar, I., Petrovic, D., Milasinovic, D., Davidovic, L., & Filipovic, N. (2014). Computer modelling of maximal displacement forces in endoluminal thoracic aortic stent graft. *Computer Methods in Biomechanics and Biomedical Engineering*, **17**(9), 1012–1020.

Ku, D. N., Giddens, D. P., Zarins, C. K., & Glagov, S. (1985). Pulsatile flow and atherosclerosis in the human carotid bifurcation. Positive correlation between plaque location and low oscillating shear stress. *Arteriosclerosis: An Official Journal of the American Heart Association, Inc.* **5**(3), 293–302.

Lantz, J., Renner, J., & Karlsson, M. (2011). Wall shear stress in a subject specific human aorta-influence of fluid-structure interaction. *International Journal of Applied Mechanics*, **3**(04), 759–778.

Lin, S., Han, X., Bi, Y., Ju, S., & Gu, L. (2017). Fluid-structure interaction in abdominal aortic aneurysm: Effect of modeling techniques. *BioMed Research International*, **2017**(1), 7023078.

Madhwal, S., Rajagopal, V., Bhatt, D. L., Bajzer, C. T., Whitlow, P., & Kapadia, S. R. (2008). Predictors of difficult carotid stenting as determined by aortic arch angiography. *The Journal of Invasive Cardiology*, **20**(5), 200–204.

Mandigers, T. J., Ramella, A., Bissacco, D., Domanin, M., van Herwaarden, J. A., Heijmen, R., Luraghi, G., Migliavacca, F., & Trimarchi, S. (2023). Thoracic stent graft numerical models to virtually simulate thoracic endovascular aortic repair: A scoping review. *European Journal of Vascular and Endovascular Surgery*, **66**(6), 784–796.

Marrocco-Trischitta, M. M., de Beaufort, H. W., Piffaretti, G., Bonardelli, S., Gargiulo, M., Antonello, M., van Herwaarden, J. A., Boveri, S., Bellosta, R., Trimarchi, S., MALAN Collaborators,. (2020). The modified arch landing areas nomenclature predicts proximal endograft failure after thoracic endovascular aortic repair. *European Journal of Cardio-Thoracic Surgery*, **58**(2), 309–318.

Marrocco-Trischitta, M. M., de Beaufort, H. W., Secchi, F., van Bakel, T. M., Ranucci, M., Van Herwaarden, J. A., Moll, F. L., & Trimarchi, S. (2017). A geometric reappraisal of proximal landing zones for thoracic endovascular aortic repair according to aortic arch types. *Journal of Vascular Surgery*, **65**(6), 1584–1590.

Marrocco-Trischitta, M. M., Melissano, G., Kahlberg, A., Calori, G., Setacci, F., & Chiesa, R. (2009). Chronic kidney disease classification stratifies mortality risk after elective stent graft repair of the thoracic aorta. *Journal of Vascular Surgery*, **49**(2), 296–301.

Marrocco-Trischitta, M. M., Romarowski, R. M., de Beaufort, H. W., Conti, M., Vitale, R., Secchi, F., Auricchio, F., & Trimarchi, S. (2019). The modified arch landing areas nomenclature identifies hostile zones for endograft deployment: A confirmatory biomechanical study in patients treated by thoracic endovascular aortic repair. *European Journal of Cardio-Thoracic Surgery*, **55**(5), 990–997.

Marrocco-Trischitta, M. M., van Bakel, T. M., Romarowski, R. M., de Beaufort, H. W., Conti, M., van Herwaarden, J. A., Moll, F. L., Auricchio, F., & Trimarchi, S. (2018). The modified arch landing areas nomenclature (MALAN) improves prediction of stent graft displacement forces: proof of concept by computational fluid dynamics modelling. *European Journal of Vascular and Endovascular Surgery*, **55**(4), 584–592.

Melissano, G., Civilini, E., Bertoglio, L., Calliari, F., Setacci, F., Calori, G., & Chiesa, R. (2007). Results of endografting of the aortic arch in different landing zones. *European Journal of Vascular and Endovascular Surgery*, **33**(5), 561–566.

Mendez, V., Di Giuseppe, M., & Pasta, S. (2018). Comparison of hemodynamic and structural indices of ascending thoracic aortic aneurysm as predicted by 2-way FSI, CFD rigid wall simulation and patient-specific displacement-based FEA. *Computers in Biology and Medicine*, **100**, 221–229.

Milewski, R. K., Szeto, W. Y., Pochettino, A., Moser, G. W., Moeller, P., & Bavaria, J. E. (2010). Have hybrid procedures replaced open aortic arch reconstruction in high-risk patients? A comparative study of elective open arch debranching with endovascular stent graft placement and conventional elective open total and distal aortic arch reconstruction. *The Journal of Thoracic and Cardiovascular Surgery*, **140**(3), 590–597.

Moireau, P., Xiao, N., Astorino, M., Figueroa, C. A., Chapelle, D., Taylor, C. A., & Gerbeau, J.-F. (2012). External tissue support and fluid-structure simulation in blood flows. *Biomechanics and Modeling in Mechanobiology*, **11**, 1–18.

Molony, D. S., Callanan, A., Kavanagh, E. G., Walsh, M. T., & McGloughlin, T. M. (2009). Fluid-structure interaction of a patient-specific abdominal aortic aneurysm treated with an endovascular stent-graft. *Biomedical Engineering Online*, **8**, 1–12.

Mourato, A., Valente, R., Xavier, J., Brito, M., Avril, S., da Sa, J. C., Tomas, A., & Fragata, J. (2022). Computational modelling and simulation of fluid structure interaction in aortic aneurysms: A systematic review and discussion of the clinical potential. *Applied Sciences*, **12**(16), 8049.

Mutlu, O., Salman, H. E., Al-Thani, H., El-Menyar, A., Qidwai, U. A., & Yalcin, H. C. (2023). How does hemodynamics affect rupture tissue mechanics in abdominal aortic aneurysm: Focus on wall shear stress derived parameters, time-averaged wall shear stress, oscillatory shear index, endothelial cell activation potential, and relative residence time. *Computers in Biology and Medicine*, **154**, 106609.

Nicoud, F., Toda, H. B., Cabrit, O., Bose, S., & Lee, J. (2011). Using singular values to build a subgrid-scale model for large eddy simulations. *Physics of fluids*, **23**(8), 085106.

Nobile, F., Pozzoli, M., & Vergara, C. (2013). Time accurate partitioned algorithms for the solution of fluid–structure interaction problems in haemodynamics. *Computers & Fluids*, **86**, 470–482.

Nobile, F., & Vergara, C. (2008). An effective fluid-structure interaction formulation for vascular dynamics by generalized robin conditions. *Society for Industrial and Applied Mathematics Journal on Scientific Computing*, **30**(2), 731–763.

Numata, S., Itatani, K., Kanda, K., Doi, K., Yamazaki, S., Morimoto, K., Manabe, K., Ikemoto, K., & Yaku, H. (2016). Blood flow analysis of the aortic arch using computational fluid dynamics. *European Journal of Cardio-Thoracic Surgery*, **49**(6), 1578–1585.

Ong, C., Kabinejadian, F., Xiong, F., Wong, Y., Toma, M., Nguyen, Y., Chua, K., Cui, F., Ho, P., & Leo, H. (2019). Pulsatile flow investigation in development of thoracic aortic aneurysm: An in-vitro validated fluid structure interaction analysis. *Journal of Applied Fluid Mechanics*, **12**(6), 1855–1872.

Ong, C. W., Yap, C. H., Kabinejadian, F., Nguyen, Y. N., Cui, F., Chua, K. J., Ho, P., & Leo, H. L. (2018). Association of hemodynamic behavior in the thoracic aortic aneurysm to the intraluminal thrombus prediction: A two-way fluid structure coupling investigation. *International Journal of Applied Mechanics*, **10**(04), 1850035.

Pantos, I., Patatoukas, G., Efstathopoulos, E. P., & Katritsis, D. (2007). In vivo wall shear stress measurements using phase-contrast MRI. *Expert review of Cardiovascular Therapy*, **5**(5), 927–938.

Pasta, S., Rinaudo, A., Luca, A., Pilato, M., Scardulla, C., Gleason, T. G., & Vorp, D. A. (2013). Difference in hemodynamic and wall stress of ascending thoracic aortic aneurysms with bicuspid and tricuspid aortic valve. *Journal of Biomechanics*, **46**(10), 1729–1738.

Peattie, R. A., Riehle, T. J., & Bluth, E. I. (2004). Pulsatile flow in fusiform models of abdominal aortic aneurysms: Flow fields, velocity patterns and flow-induced wall stresses. *Journal of Biomechanical Engineering*, **126**(4), 438–446.

Piccinelli, M., Vergara, C., Antiga, L., Forzenigo, L., Biondetti, P., & Domanin, M. (2013). Impact of hemodynamics on lumen boundary displacements in abdominal aortic aneurysms by means of dynamic computed tomography and computational fluid dynamics. *Biomechanics and Modeling in Mechanobiology*, **12**, 1263–1276.

Powell, A., Maier, S., Chung, T., & Geva, T. (2000). Phase-velocity cine magnetic resonance imaging measurement of pulsatile blood flow in children and young adults: In vitro and in vivo validation. *Pediatric Cardiology*, **21**, 104–110.

Pozzi, S., Domanin, M., Forzenigo, L., Votta, E., Zunino, P., Redaelli, A., & Vergara, C. (2021). A surrogate model for plaque modeling in carotids based on robin conditions calibrated by cine MRI data. *International Journal for Numerical Methods in Biomedical Engineering*, **37**(5), e3447.

Quarteroni, A., Manzoni, A., & Vergara, C. (2017). The cardiovascular system: Mathematical modelling, numerical algorithms and clinical applications. *Acta Numerica*, **26**, 365–590.

Regazzoni, F., Salvador, M., Africa, P. C., Fedele, M., Dedè, L., & Quarteroni, A. (2022). A cardiac electromechanical model coupled with a lumped-parameter model for closed-loop blood circulation. *Journal of Computational Physics*, **457**, 111083.

Reymond, P., Crosetto, P., Deparis, S., Quarteroni, A., & Stergiopulos, N. (2013). Physiological simulation of blood flow in the aorta: Comparison of hemodynamic indices as predicted by 3-D FSI, 3-D rigid wall and 1-D models. *Medical Engineering & Physics*, **35**(6), 784–791.

Riambau, V., Böckler, D., Brunkwall, J., Cao, P., Chiesa, R., Coppi, G., Czerny, M., Fraedrich, G., Haulon, S., Jacobs, M., Lachat M. L., Moll F. L., Setacci C., Taylor P. R., Thompson M., Trimarchi S., Verhagen H. J., & Verhoeven E. L., ESVS Guidelines Committee. Schmidli. (2017). Editor's choice–management of descending thoracic aorta diseases: Clinical practice guidelines of the European Society for Vascular Surgery (ESVS). *European Journal of Vascular and Endovascular Surgery*, **53**(1), 4–52.

Romarowski, R. M., Lefieux, A., Morganti, S., Veneziani, A., & Auricchio, F. (2018). Patient-specific CFD modelling in the thoracic aorta with pc-MRI-based boundary conditions: A least-square three-element Windkessel approach. *International Journal for Numerical Methods in Biomedical Engineering*, **34**(11), e3134.

Scotti, C. M., Shkolnik, A. D., Muluk, S. C., & Finol, E. A. (2005). Fluid-structure interaction in abdominal aortic aneurysms: Effects of asymmetry and wall thickness. *Biomedical Engineering Online*, **4**, 1–22.

Shamanskiy, A., & Simeon, B. (2021). Mesh moving techniques in fluid-structure interaction: Robustness, accumulated distortion and computational efficiency. *Computational Mechanics*, **67**(2), 583–600.

Shang, E. K., Nathan, D. P., Sprinkle, S. R., Vigmostad, S. C., Fairman, R. M., Bavaria, J. E., Gorman, R. C., Gorman, J. H. III, Chandran, K. B., & Jackson, B. M. (2013). Peak wall stress predicts expansion rate in descending thoracic aortic aneurysms. *The Annals of Thoracic Surgery*, **95**(2), 593–598.

Silva, M. L. F. D., Gonçalves, S. D. F., Haniel, J., Lucas, T. C., & Huebner, R. (2023). Comparative study between 1-way and 2-way coupled fluid-structure interaction in numerical simulation of aortic arch aneurysms. *Anais da Academia Brasileira de Ciências*, **95**(S1), e20210859.

Soudah, E., Ng, E., Loong, T., Bordone, M., Pua, U., & Narayanan, S. (2013). CFD modelling of abdominal aortic aneurysm on hemodynamic loads using a realistic geometry with CT. *Computational and Mathematical Methods in Medicine*, **2013**(1), 472564.

Tan, F., Borghi, A., Mohiaddin, R., Wood, N., Thom, S., & Xu, X. (2009). Analysis of flow patterns in a patient-specific thoracic aortic aneurysm model. *Computers & Structures*, **87**(11-12), 680–690.

Tan, F., Torii, R., Borghi, A., Mohiaddin, R., Wood, N., & Xu, X. (2009). Fluid-structure interaction analysis of wall stress and flow patterns in a thoracic aortic aneurysm. *International Journal of Applied Mechanics*, **1**(01), 179–199.
Thomas, B., & Sanchez, L. (2009). Proximal migration and endoleak: Impact of endograft design and deployment techniques. *Seminars in Vascular Surgery*, **22**, 201–206.
Tse, K. M., Chiu, P., Lee, H. P., & Ho, P. (2011). Investigation of hemodynamics in the development of dissecting aneurysm within patient-specific dissecting aneurismal aortas using computational fluid dynamics (CFD) simulations. *Journal of Biomechanics*, **44**(5), 827–836.
Valente, R., Mourato, A., Brito, M., Xavier, J., Tomás, A., & Avril, S. (2022). Fluid-structure interaction modeling of ascending thoracic aortic aneurysms in simvascular. *Biomechanics*, **2**(2), 189–204.
Van de Vosse, F., De Hart, J., Van Oijen, C., Bessems, D., Gunther, T., Segal, A., Wolters, B., Stijnen, J., & Baaijens, F. (2003). Finite-element-based computational methods for cardiovascular fluid-structure interaction. *Journal of Engineering Mathematics*, **47**, 335–368.
Van Prehn, J., Vincken, K., Sprinkhuizen, S., Viergever, M., Van Keulen, J., Van Herwaarden, J., Moll, F., & Bartels, L. (2009). Aortic pulsatile distention in young healthy volunteers is asymmetric: Analysis with ECG-gated MROI. *European Journal of Vascular and Endovascular Surgery*, **37**(2), 168–174.
Van Puyvelde, J., Verbeken, E., Verbrugghe, P., Herijgers, P., & Meuris, B. (2016). Aortic wall thickness in patients with ascending aortic aneurysm versus acute aortic dissection. *European Journal of Cardio-Thoracic Surgery*, **49**(3), 756–762.
Venkatasubramaniam, A., Fagan, M., Mehta, T., Mylankal, K., Ray, B., Kuhan, G., Chetter, I., & McCollum, P. (2004). A comparative study of aortic wall stress using finite element analysis for ruptured and non-ruptured abdominal aortic aneurysms. *European Journal of Vascular and Endovascular Surgery*, **28**(2), 168–176.
Vergara, C., Le Van, D., Quadrio, M., Formaggia, L., & Domanin, M. (2017). Large Eddy simulations of blood dynamics in abdominal aortic aneurysms. *Medical Engineering & Physics*, **47**, 38–46.
Vorp, D. A., Raghavan, M., & Webster, M. W. (1998). Mechanical wall stress in abdominal aortic aneurysm: Influence of diameter and asymmetry. *Journal of Vascular Surgery*, **27**(4), 632–639.
Vorp, D. A., Schiro, B. J., Ehrlich, M. P., Juvonen, T. S., Ergin, M. A., & Griffith, B. P. (2003). Effect of aneurysm on the tensile strength and biomechanical behavior of the ascending thoracic aorta. *The Annals of Thoracic Surgery*, **75**(4), 1210–1214.
Wang, X., Ghayesh, M. H., Kotousov, A., Zander, A. C., Dawson, J. A., & Psaltis, P. J. (2023). Fluid–structure interaction study for biomechanics and risk factors in Stanford type A aortic dissection. *International Journal for Numerical Methods in Biomedical Engineering*, **39**(8), e3736.
Westerhof, N., Lankhaar, J.-W., & Westerhof, B. E. (2009). The arterial windkessel. *Medical & Biological Engineering & Computing*, **47**(2), 131–141.
Wilcox, D. C. (1998). *Turbulence modeling for CFD* (Vol. **2**). DCW Industries.
Wolters, B., Rutten, M., Schurink, G., Kose, U., De Hart, J., & Van De Vosse, F. (2005). A patient-specific computational model of fluid–structure interaction in abdominal aortic aneurysms. *Medical Engineering & Physics*, **27**(10), 871–883.
Zeng, Y.-Q., & Li, Z.-Y. (2013). A follow up MRI-based geometry and computational fluid dynamics study of carotid bifurcation. In *World congress on medical physics and biomedical engineering, May 26–31, 2012, Beijing, China* (pp. 172–175). Springer.

Additional information

Data availability statement

All data supporting the results of this work are available within the published article.

Competing interests

The authors declare no competing interests.

Author contributions

All clinical data were acquired at Section of Vascular Surgery, Cardio Thoracic Vascular Department, Fondazione I.R.C.C.S. Ca' Granda Ospedale Maggiore Policlinico, Milan, Italy. All the computational simulations were performed at LaBS, Dipartimento di Chimica, Materiali e Ingegneria Chimica, Politecnico di Milano, Milan, Italy. F.D.: conceptualization of the work, development of methodology, code development, image reconstruction, numerical simulations, postprocessing of the results, interpretation of the results, writing of the original draft, editing of the final version of the manuscript. D.B.: conceptualization of the work, acquisition of the clinical data, interpretation of the results, revision of the manuscript. L.C.: development of methodology, code development, revision of the manuscript. C.F.: development of methodology, code development, revision of the manuscript. M.D.: conceptualization of the work, acquisition of the clinical data, interpretation of the results, revision of the manuscript. F.M.: conceptualization of the work, interpretation of the results, revision of the manuscript, supervision, funding acquisition. S.T.: conceptualization of the work, acquisition of the clinical data, interpretation of the results, revision of the manuscript. C.V.: conceptualization of the work, development of methodology, interpretation of the results, editing of the final version of the manuscript, supervision, funding acquisition. All authors have approved the final version of the manuscript and agree to be accountable for all aspects of the work. All persons designated as authors qualify for authorship, and all those who qualify for authorship are listed.

Funding

This study received funding from the European Union-Next Generation EU, Mission 4, Component 1, CUP: D53D23014380006, under the research project MIUR PRIN22 n.2022L3JC5T, 'Predicting the outcome of end-ovascular repair for thoracic aortic aneurysms: analysis of fluid dynamic modelling in different anatomical settings and clinical validation'.

Acknowledgements

F.D., C.V. and L.C. are members of the INdAM group GNCS 'Gruppo Nazionale per il Calcolo Scientifico' (National Group for Scientific Computing). C.V. has been partially supported by (i) the European Union-Next Generation EU, Mission 4, Component 1, CUP: D53D23018770001, under the research project MIUR PRIN22-PNRR n. P20223KSS2, 'Machine learning for fluid structure interaction in cardio-vascular problems: efficient solutions, model reduction, inverse problems'; (ii) the Italian Ministry of Health within the PNC PROGETTO HUB LIFE SCIENCE – DIAGNOSTICA AVANZATA (HLS-DA) 'INNOVA', PNCE3-2022-23683266, CUP: D43C22004930001, within the 'Piano Nazionale Complementare Ecosistema Innovativo della Salute', Codice univoco investimento: PNCE3-2022-23683266; (iii) Italian Ministry of Health within the project 'CAL.HUB.RIA' – CALABRIA HUB PER RICERCA INNOVATIVA ED AVANZATA, Code: T4-AN-09, CUP: F63C22000530001.

Keywords

drag forces, fluid–structure interaction, landing zones, TEVAR, thoracic aortic aneurysm

Supporting information

Additional supporting information can be found online in the Supporting Information section at the end of the HTML view of the article. Supporting information files available:

Peer Review History